

**Surface Chemistry of Norbornadiene/Quadricyclane  
as Energy Storage System Studied by *In Situ*  
Photoemission Techniques**

Oberflächenchemie von Norbornadien/Quadricyclan  
als Energiespeichersystem untersucht mit  
*in situ* Photoemissionsmethoden

Der naturwissenschaftlichen Fakultät  
der Friedrich-Alexander-Universität Erlangen-Nürnberg

zur Erlangung des Doktorgrades Dr. rer. nat.

vorgelegt von

**Udo Bauer**

aus Gunzenhausen

Als Dissertation genehmigt  
von der Naturwissenschaftlichen Fakultät  
der Friedrich-Alexander-Universität Erlangen-Nürnberg

Tag der mündlichen Prüfung:

Vorsitzender des  
Promotionsorgans:

Gutachter:           Prof. Dr. Hans-Peter Steinrück  
                          Prof. Dr. Andreas Hirsch

## Contents

1	Introduction .....	1
1.1	Norbornadiene/quadricyclane as molecular solar thermal system .....	1
1.2	Catalyst modification: Pt <sub>x</sub> Ag <sub>1-x</sub> /Pt(111) and C/Mo(110).....	5
2	Fundamentals and theoretical background .....	9
2.1	Synchrotron-based radiation .....	9
2.2	X-ray photoelectron spectroscopy (XPS) and ultraviolet photoelectron spectroscopy (UPS).....	11
2.3	Near edge X-ray absorption fine structure (NEXAFS) .....	19
2.4	Temperature-programmed desorption (TPD) .....	22
3	Experimental setup .....	25
3.1	Synchrotron UHV setup .....	25
3.2	TPD UHV Setup .....	27
4	Surface chemistry of norbornadiene/quadricyclane .....	29
4.1	Reaction of NBD/QC on Pt(111) <sup>[P1]</sup> .....	29
4.2	Reaction of NBD/QC on Ni(111) <sup>[P2]</sup> .....	34
4.3	Reaction of 2,3-dibromosubstituted NBD/QC on Ni(111) <sup>[P3]</sup> .....	38
5	Catalyst modification.....	43
5.1	Reaction of CO and C <sub>2</sub> H <sub>4</sub> on bimetallic Pt <sub>x</sub> Ag <sub>1-x</sub> /Pt(111) surface alloys <sup>[P4]</sup> .....	43
5.2	Reaction of C <sub>2</sub> H <sub>4</sub> , C <sub>6</sub> H <sub>6</sub> and C <sub>6</sub> H <sub>12</sub> on C/Mo(110) <sup>[P5]</sup> .....	46
6	Summary.....	51
7	Zusammenfassung .....	55

8	Literature .....	59
9	Danksagung .....	67
10	Curriculum vitae .....	69
A	Appendix [P1-P5] .....	71
B	Appendix .....	B1

# 1 Introduction

## 1.1 Norbornadiene/quadricyclane as molecular solar thermal system

The search for and development of alternative and especially green energy production concepts will be a key aspect of the 21st century. At the moment, the world's energy consumption is based to about 87% on fossil fuels (coal, oil and gas) and just to 1.6% on renewables (sunlight, wind, tide, geothermal heat).<sup>1-2</sup> Despite the advantages like easy accessibility and high gravimetric and volumetric storage densities<sup>3</sup>, fossil fuels will be exhausted in the medium-term future. Experts are talking about 153, 51 and 53 years for coal, oil and gas, respectively, based on the reserves-to-production ratios in 2017, and not considering unexplored deposits.<sup>4</sup> Even more dramatically is the CO<sub>2</sub> emission that occurs with every burning process of the mentioned fuels due to its potential as greenhouse gas leading to increasing temperature, which again engenders a higher CO<sub>2</sub> concentration in the atmosphere as gas solubility of the oceans decreases with increasing temperature. To break up with this vicious circle, humanity is forced, at least by moral attitude if not from politics, to invest into renewable energy routes beyond fossil fuels. The major issue with technologies like the already established photovoltaic systems, wind power plants and also barely used sources like geothermics or tidal power, is the fact that they all suffer from either seasonal, climatic or geographic dependence, which makes an independent energy supply and closed network without fossil fuels a very challenging goal. However, this goal could be reached with renewables that will become more and more affordable, but the energy distribution will inevitably need storage systems.<sup>5-6</sup> Nowadays, about 99% of electrical energy storage is performed via pumped hydro storage systems whereas other ways like compressed air and batteries only play a very minor role.<sup>7-8</sup> With growing proportion of renewables and associated fluctuating energy supply, demanding periods can by far not be compensated only by additional pumped storage hydropower stations as natural terrain does not provide enough locations. Here, a strong need for innovative storage methods arises, especially for large scale applications like residential and economic supply.

Among the four possible classifications which are mechanical, electrical, electrochemical and chemical storage, the latter one is a very promising approach receiving increasing research interest. The basic idea for chemical energy storage is either to photochemically produce compounds that hold large amounts of energy to be combusted such as methanol and hydrogen or to harvest sunlight directly for a switchable photosystem that stores energy in form of chemical bonds, as the sun is by far the most accessible energy source on our planet. Both approaches generate solar fuels in numerous variants. In case of hydrogen production, nature acts as a model when artificial photosynthesis, meaning the production of hydrogen and oxygen gas out of water, is performed. Despite the engineering part of such a solar fuel cell, the search for an efficient light harvesting unit, the photocatalyst, and an earth-abundant material performing as electrocatalyst, is of utmost importance. Of course, there is a large variety of approaches and investigations in this field in the literature concerning, e.g., tailoring the catalysts, practical application in devices or biomimicking nature's photosystem I and II catalysts.<sup>9-17</sup>

As a next step, the generated hydrogen can be utilized in different fields such as fuel cells where it gets combusted to water under enthalpy release, and photocatalytic reduction of CO<sub>2</sub> to methane and methanol as valuable solar fuels.<sup>18-22</sup> A rather new concept are liquid organic hydrogen carriers (LOHCs) where hydrogen is chemically bound and can be stored over large periods with a high energy density.<sup>3,23-27</sup> Switchable photosystems, which will be followed in this thesis, store absorbed energy from sunlight directly in form of chemical bonds or chemical strain. Principally, three different systems are reported: the cis-trans isomerization of azobenzene<sup>28-33</sup>, stilbene<sup>28,34-35</sup> and anthracene<sup>34,36-37</sup> derivatives, the constitutional isomerization of fulvalene-tetracarbonyl-diruthenium complexes<sup>38-43</sup>, and the intramolecular [2+2] cycloaddition of norbornadiene (NBD) to quadricyclane (QC), see Figure 1.1. The latter system has already been studied decades ago including pioneer work on photochemical properties.<sup>44-54</sup> As norbornadienes exhibit higher energy storage densities compared to azobenzenes, stilbenes and anthracenes (e.g., norbornadiene: ~966-1093 kJ kg<sup>-1</sup><sup>52,54</sup> and azobenzene: ~269 kJ kg<sup>-1</sup><sup>55</sup>), and ruthenium complexes are too expensive due to their content of rare noble metal, the NBD/QC system seems currently to be the most promising candidate for future applications. Several key parameters have to be investigated and tailored for such a so-called MOST (molecular solar thermal) system to become available and profitable for large scale application. Despite the demand for cheap, non-toxic and easy manageable chemicals, it is obvious that high enough energy storage densities

have to be achieved, which of course is directly related to the molecular weight of the compounds. The parent NBD compound can store  $\sim 89\text{--}96\text{ kJ mol}^{-1}$  resp.  $\sim 1000\text{ kJ kg}^{-1}$ , which is indeed rather low in comparison to, e.g., gasoline with about  $47 \cdot 10^3\text{ kJ kg}^{-1}$ <sup>56</sup>. However, one has to keep in mind that solar fuels are sustainable energy sources and when compared to, e.g., Li-ion batteries ( $\sim 720\text{ kJ kg}^{-1}$ <sup>56</sup>) they perform quite well. Unfortunately, a limiting factor of NBD/QC is that up to now the stored energy can only be released as heat in a profitable way. For

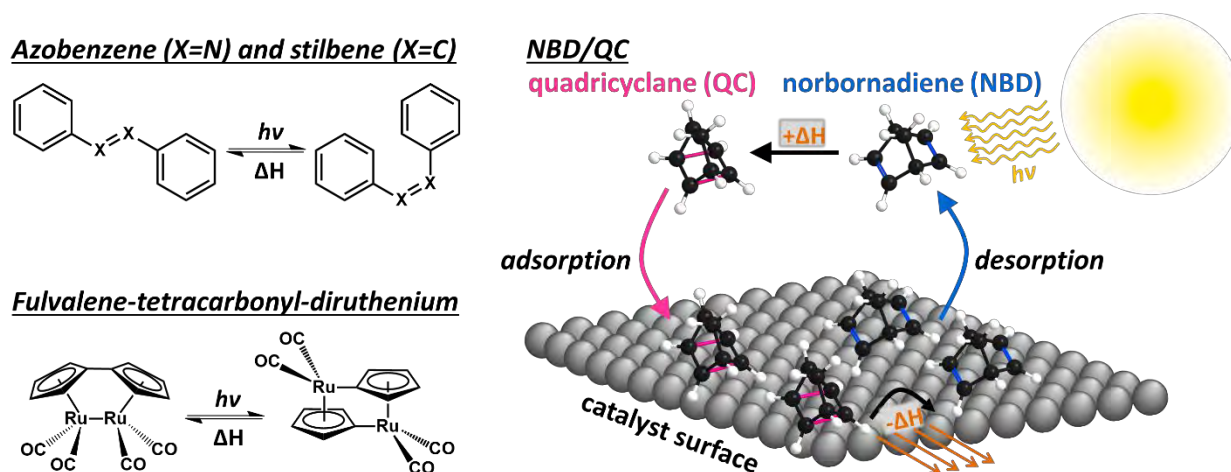


**Figure 1.1:** Different types of molecular solar thermal (MOST) energy storage systems.

this, a threshold of  $\sim 300\text{ kJ kg}^{-1}$  during the cycloreversion from QC to NBD should at least be overcome to exceed the energy stored by solar warming of water with  $\Delta T = 50\text{ K}$ .<sup>52</sup> Secondly, the NBD compound must absorb in the near-UV and visible region (300 – 700 nm), since over 50% of sunlight's power that reaches the earth is distributed in this range. Underivatized NBD has its absorption maximum at  $\sim 310\text{ nm}$ , consequently an absorption red-shift is desired. On the other hand, the energy-loaded compound QC then should not exhibit any significant absorption bands in this region to inhibit a photoinduced back reaction, meaning it should be colorless.<sup>52</sup> This requirement is connected to another important aspect, which is the thermodynamic stability of the QC photoisomer. The activation barrier for the back reaction must be high enough to be not overcome 'accidentally' by surrounding conditions, e.g., storage temperature, which means in other words that the half-life should at least lie in a medium-term range of weeks to months. Another crucial aspect is the yield of both, the photoisomerization and the energy releasing cycloreversion. As neat NBD exhibits only a low quantum yield of 0.05<sup>52,57</sup>, strategies for increasing this value, in best case close to unity, are urgently needed. Here, two routes are

proposed. Either one utilizes transition metal complexes and salts, which form a complex with NBD that can be photoexcited to produce QC, or organic compounds, e.g., Michler's ketone (4,4'-bis(dimethylamino)benzophenone) are exploited to act as triplet sensitizers. The sensitizer gets photoexcited to a singlet state, converts to a triplet state via intersystem crossing, which then can excite NBD to a triplet state, which finally transforms into the QC ground state.<sup>52-53</sup> The cycloreversion instead needs catalysts that trigger only the back reaction and not undesired side reactions. Homo- and heterogeneous and electrochemical catalysis is reported to work for the conversion of QC to NBD.

In the following, a short review on recent published results on optimizing the NBD/QC MOST system is presented. Concerning surface science studies under ultra-high vacuum (UHV) conditions, only two publications on the adsorption and thermal stability of NBD on Pt(111) have been reported.<sup>58-59</sup> Recently, Brummel et al. showed with an electrochemical setup of Pt electrodes in a  $\text{Bu}_4\text{NClO}_4/\text{acetonitrile}$  electrolyte, that QC can be oxidized to NBD via a  $\text{QC}^{\bullet+}$  radical cation and that the kinetics can be controlled via the applied electrode potential.<sup>60</sup> The group of Moth-Poulsen et al. has searched for optimized NBD derivatives concerning the above mentioned parameters over the last few years. By introducing a cyano group as acceptor and an ethynyl linker group as donor at position C2 and C3 of the NBD parent compound, the absorption maximum undergoes a red shift of  $\sim 90$  nm whereas the molecular weight resp. the energy storage density still exhibit low resp. large values ( $260 \text{ g mol}^{-1}$ ;  $629 \text{ kJ kg}^{-1}$ ).<sup>61</sup> Furthermore, they found out that substitution at the C7 position can increase thermal lifetimes of NBD (and probably also QC) due to an increased activation entropy for the rotation of bulky functional groups at this position.<sup>62</sup> Latest results present compounds with a shear viscosity high enough for devices (e.g., combined with a solar water heating system<sup>63</sup>) to be driven without additional solvents<sup>64</sup> and recently NBD/QC oligomers have been proved to exceed energy storage densities, storage lifetimes and quantum yields of their monomeric analogs<sup>65</sup>.

The investigation of fundamental reaction and decomposition steps of the energy release from QC to NBD on catalyst surfaces plays an essential role when tailoring optimized systems. Studies with surface science tools under ultra clean UHV conditions give an insight into those processes and can help to transfer the gained knowledge on systems running under real catalytic conditions, either in a heterogeneous or electrochemical approach, where the gas- resp. liquid-

solid interface determines the reactivity.

## 1.2 Catalyst modification: $\text{Pt}_x\text{Ag}_{1-x}/\text{Pt}(111)$ and $\text{C}/\text{Mo}(110)$

Catalysis plays a key role in many industrial-scale processes that have enabled prosperity and also ensured the feeding of the growing population on earth. Sulfuric acid for example is an educt for many chemical reactions and can be produced via the contact process when  $\text{SO}_2$  is reacted with  $\text{O}_2$  with the help of  $\text{V}_2\text{O}_5$  as catalyst, which promotes the reaction to  $\text{SO}_3$ . Another example is the reaction of  $\text{N}_2$  with  $\text{H}_2$  in the Haber-Bosch process where ammonia is formed, which is the basic component of all industrially produced nitrogen-containing compounds and thus also raw material for fertilizers. Without the catalytic help of a mixture of metallic iron and iron oxides, the reaction requires enormous temperature and pressure. In other words, earth's population could have never reached 7.6 billions of people by now without a suitable catalyst for this essential reaction.

In general, catalysis is the participation of a catalyst in a reaction to increase its rate without changing the overall free enthalpy or Gibbs energy and without being consumed. Already in 1823, Johann W. Döbereiner, the German chemist and father of catalysis, recognized 'that the pure metallic and powdered platinum exhibits the highly peculiar property to govern the hydrogen gas by mere contact and without all help of outer potencies in a way that it combines to water with oxygen gas under the excitation of an increased amount of heat until burning of the platinum'.<sup>66</sup> For many chemical reactions, platinum group metals, which are ruthenium, rhodium, palladium, osmium, iridium and platinum, show a superior performance in catalysis compared to other metals or corresponding compounds of them. This correlation can be nicely seen from a volcano plot, which illustrates the Sabatier principle<sup>67-68</sup>, see Figure 1.2, on the example of formic acid decomposition on different transition metals. If the heat of formation for metal formates is too low, like it is the case for Au and Ag, the dissociative adsorption of the formic acid is the rate-limiting step and higher temperatures are required to increase the adsorption rate in order to achieve the given rate of 15% for the overall dehydrogenation. For heat of formations higher than  $\sim 350 \text{ kJ mol}^{-1}$  (valid for Cu, Ni, Co, Fe and W), the desorption is the rate-limiting step and higher temperatures are required to loosen the bond between formate and surface. Platinum group metals exhibit a medium heat of formation where the reaction rate is

a combination of the rates for ad- and desorption and thus a relatively low temperature is needed to perform the reaction. In reality, the process is more complex. The values for the heat of formation have been calculated (from standard enthalpies of formation) and the shape of the plot may look different to some extent, which will not disturb the general message of the principle. As can be seen from the model represented in Figure 1.2, all of the metals are catalytically active. So there is the possibility to either wait for longer times, increase the temperature or change the composition/morphology of the catalyst to perform the reaction faster. Since the first

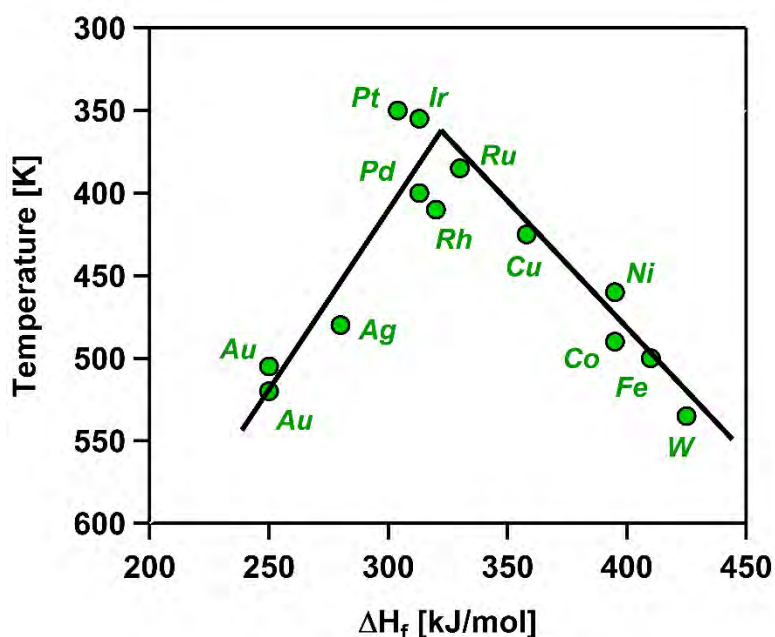


**Figure 1.2:** Volcano plot showing the relation between the calculated formation enthalpy of metal formates ( $HCOO \cdots M$ ) and the temperature at which the rate of the reaction  $HCCOH \rightarrow CO_2 + H_2$  on the corresponding metals reaches 15%. The plot is reproduced from the work of Trillo et al.<sup>69</sup>

two options are not efficient, only tailoring the catalyst itself is a practicable approach. Besides enlarging the surface area of a material, e.g., via pore size extension, one can reduce the precious metal content of a catalyst for more abundant elements. In case of platinum group metals, this is urgently required as all of the platinum group metals' abundance is smaller than 20 ppb in earth shell. Compared to iron with 4.7% or Ni with 0.15%, those values are simply not large enough to supply all catalysts with precious metals.

Precious metal content reduction can be achieved via the formation of alloys. Bimetallic alloys exhibit interesting new physical and chemical properties concerning catalysis.<sup>70-75</sup> In literature, many examples of such alloys are reported where the catalytic performance of the parent metal is even exceeded. One example is the usage of Pt<sub>3</sub>M (M = Ni, Co, Fe, Ti, V) in the electrochemical oxygen-reduction reaction ( $\frac{1}{2}\text{O}_2 + 2\text{H}^+ + 2\text{e}^- \rightarrow \text{H}_2\text{O}$ ) at the cathode of an oxygen-hydrogen fuel cell. Here, Pt<sub>3</sub>Fe alloy surfaces show a larger activity than pure polycrystalline Pt samples.<sup>76</sup> Generally, the altered activity of alloy surfaces can be explained by 4 effects: (1) site blocking of specific sites by innocent metal atoms, (2) strain effects due to different lattice constants, (3) geometric ensemble effects, which arise due to the spatial distribution of atoms, and (4) electronic ligand effects. The latter one has the biggest influence in most cases, because the d-band center of the reactive metal atoms gets shifted or changes in width when in neighborhood to the other sort of metal atoms; this can result in changed adsorption energies.<sup>77-79</sup>

Another method to avoid precious metals for catalysts has been discovered in 1973 by Levy and Boudart.<sup>80</sup> They observed the platinum-like behavior of tungsten carbide in reactions like water formation from hydrogen and oxygen at room temperature or isomerization of 2,3-dimethylpropane to 2-methylbutane. With this study, the investigation on early transition metal carbides as potential catalysts has started and their application has become popular in many fields.<sup>81-84</sup> Especially, molybdenum carbide surfaces have been investigated in detail<sup>85-90</sup> due to their similar behavior to platinum in, e.g., dehydrogenation and oxidation reactions.<sup>91-92</sup>

This dissertation is written in a cumulative form which is based on five publications. Four of them have already been published ([P1], [P2], [P4] and [P5]) and one ([P3]) is close to submission. I am the first author of [P3]-[P5] and I share first authorship for [P1] and [P2]. Publications [P1]-[P3] have been performed in collaboration with the groups of Prof. Dr. Andreas Hirsch, Prof. Dr. Andreas Görling and Prof. Dr. Jörg Libuda. In these publications, I have performed all XPS, UPS and NEXAFS measurements, evaluated the data and written the corresponding parts in the publication script including the complete introduction and conclusion. The organic NBD and QC compounds have been synthesized by the group of Prof. Dr. Andreas Hirsch. All DFT (density functional theory) calculations and simulations resp. IRAS (infrared reflection absorption spectroscopy) measurements have been performed by the group of Prof. Dr.

Andreas Görling resp. Prof. Dr. Jörg Libuda, including the writing of the corresponding parts in the scripts. All data acquisition, evaluation and script writing of publication [P4] and [P5] have been performed by myself.

In the following chapter, a brief description of the applied scientific tools and corresponding fundamentals is presented, and in Chapter 3 the experimental setup is explained. Afterwards, the main results on the NBD/QC MOST system and on the modified catalyst systems are addressed in Chapter 4 resp. 5 according to the corresponding publications. The last two Chapters 6 and 7 summarize the thesis, first in English followed by a German translation. Finally, an Appendix is attached which contains the publications including supporting information in part A, and in part B, a description and practical instruction on a self-built UHV UV LED, and UV irradiation reaction vessel, which can be employed to prepare QC and its derivatives, is presented.

## 2 Fundamentals and theoretical background

### 2.1 Synchrotron-based radiation

All the presented XPS data has been measured at the synchrotron facility BESSY II of Helmholtz-Zentrum Berlin. Thus, a brief description of synchrotron radiation generation and its properties is given in this chapter. The spectral range of synchrotron radiation extends from infrared light to hard X-rays, that is wavelengths from  $\sim 10^{-3}$  to  $10^{-13}$  m, resp. photon energies from  $\sim 10^{-3}$  to  $10^7$  eV. This implicates that a broad field of applications can be addressed by various spectroscopic tools. Determination of band structures in solids for semiconductor materials, macromolecular structure of proteins or the atomic structure of matter are just examples showing the importance of synchrotron radiation in science.<sup>93</sup>

Synchrotron radiation is generated when charged particles are accelerated to relativistic speed and forced into a curved motion by electric or magnetic fields.<sup>94</sup> Typical kinetic particle energies  $E_{kin}$  are between MeV and GeV, calculated by

$$E_{kin} = \frac{m_0 c^2}{\sqrt{1 - v^2/c^2}} \quad (1)$$

with  $c$  being the speed of light,  $m_0$  the rest mass and  $v$  the velocity of the particle. If accelerated, these particles emit electromagnetic radiation, with a power of radiation  $P_r$  of<sup>93</sup>

$$P_r = \frac{c q^2 E_{kin}^4}{6\pi \epsilon_0 r^2 (m_0 c^2)^4} \quad (2)$$

with  $q$  being the charge of the particle,  $\epsilon_0$  the dielectric constant and  $r$  the orbit radius of the particle's motion. It is obvious from equation (2) that protons are normally not chosen as charged particles since their rest mass is far too large, leading to a drastic reduction of the emitted power. Moreover, electrons are favored over positrons as their generation is too sophisticated, whereas electrons can be produced with a simple hot cathode.

Basically, the setup for synchrotron radiation always consists of two parts, a pre-accelerating unit and a large storage ring, see a schematic picture of the storage ring BESSY II in

Figure 2.1. Pre-acceleration is achieved electrostatically to some hundreds of keV followed by linear acceleration. So-called cavities, which are hollow resonators, with a time-dependent (oscillating) electric field inside, further accelerate temporarily separated bunches of electrons. Nowadays, in modern facilities, a synchrotron is used (instead of many linear cavities) for final acceleration before injecting the electron bunches into the storage ring. This setup is more

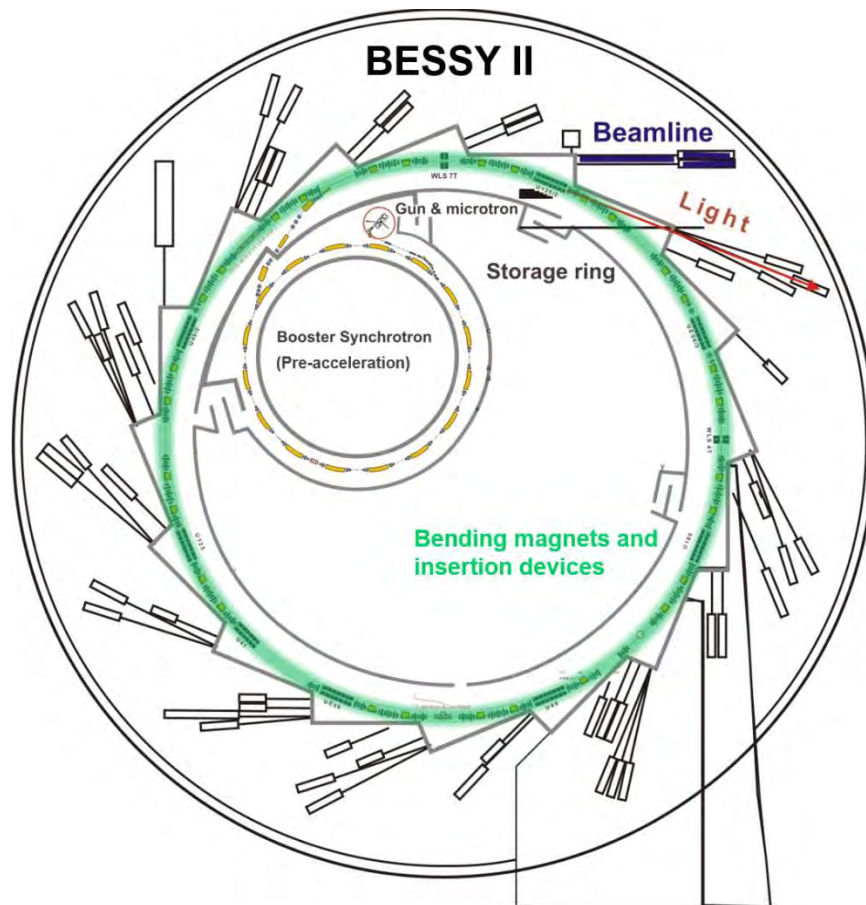


**Figure 2.1:** Schematic view of the storage ring BESSY II of Helmholtz-Zentrum Berlin. The picture is reproduced from the HZB website.<sup>95</sup>

efficient, as the bunches move on a circular orbit and each cavity can accelerate a bunch several times. To hold the bunches in the orbit, a system of magnetic fields, dependent on the electron energy, is necessary. When acceleration is completed, the bunches are injected into the storage ring itself, which in principle is a large synchrotron. Also here, cavities are needed for continuous energy input, as the particles lose energy due to the emitted synchrotron radiation with each circulation. The radiation itself in the storage ring is generated either via bending

magnets (1<sup>st</sup> generation) or so-called insertion devices which are wigglers (2<sup>nd</sup> generation) and undulators (3<sup>rd</sup> generation). Both, wigglers and undulators work according to the same principle. The electron bunches are deflected on an oscillating trajectory through several dipole magnets with alternating orientation. However, for undulators the amplitude is way smaller leading to interference phenomena (constructive and destructive) of the wavefronts, and thus larger radiation intensity is emitted. For wigglers, the intensity  $I$  depends on the number of poles  $N$  like  $I \sim N$ , whereas for undulators,  $I \sim N^2$  is found. A monochromator, whose parameters have to be set simultaneously with the undulator, ensures exact radiation energies with narrow linewidth for the users. Finally, the beam gets focused at the end stations (beamlines) with the help of a system of mirrors.

Performing experiments at synchrotrons offers several advantages. The possibility to change the energy of the exciting photons not only offers access to a broad field of spectroscopic tools, but it even extends possibilities and allows for new methods. For example, photoemission studies can be performed extremely surface sensitive due to the information depth dependency on the kinetic energy of emitted photoelectrons. Near edge X-ray absorption fine structure spectroscopy can only be performed at a synchrotron, because a continuous variation of the photon energy is necessary. Another important advantage is the high photon flux of synchrotrons which increases the signal-to-noise ratio of measured data and thus measurement times can be reduced. Finally, comprehensive experiments can be conducted under constant conditions without disruption at synchrotrons, as lifetimes of the particle bunches in a storage ring are commonly in the order of several hours ( $\sim 2$ -50 h) or the ring current is kept constant (top-up mode).

## **2.2 X-ray photoelectron spectroscopy (XPS) and ultraviolet photoelectron spectroscopy (UPS)**

The fundamentals of photoemission techniques go back to the discoveries of Hertz in 1887 when he observed that illuminating a negative electrode by UV light facilitates a spark between two electrodes.<sup>96</sup> Of course, he was not able to explain his findings as the concept of the electron has not yet been described at this time. In 1905, Einstein invoked the quantum nature of

light and delivered the qualitative and quantitative description of the photoelectric effect Hertz observed almost 20 years before.<sup>97</sup> After further development in the field of X-ray spectroscopy, Siegbahn and co-workers smoothed the way in the 1970s for conventional XPS setups as analysis tool.<sup>98</sup> At this time, the term ESCA (electron spectroscopy for chemical analysis) has been invented, and nowadays, XPS is a widely used and extremely powerful analysis tool in many fields of science.

The photoelectric effect is the phenomenon when an atom absorbs high-energy electromagnetic radiation of energy  $h\nu$  after which a core or valence electron with binding energy  $E_B$  can be ejected with a kinetic energy of

$$E_{kin} = h\nu - E_B - \varphi_S \quad (3)$$

with  $h$  being the Planck constant,  $\nu$  the radiation frequency and  $\varphi_S$  the work function of the investigated material. Equation (3) gives the kinetic energy  $E_{kin}$  an emitted electron can obtain without losing energy in secondary processes like Auger excitation (see later in this chapter) or inelastic scattering during the photoemission process. The binding energy  $E_B$  is the energy difference between the excited niveau and the highest occupied state, which is the Fermi level. The work function  $\varphi_S$ , being the difference between Fermi level and vacuum level, is a material's surface property and generally not known (or measured) as it depends on the crystal facet and contamination. Thus, the Fermi level is taken as reference resp. zero point for  $E_{kin}$ . As one measures the kinetic energy referenced to the analyzer, which also exhibits a work function  $\varphi_A$ , equation (3) changes to

$$E_{kin} = h\nu - E_B - \varphi_A. \quad (4)$$

In case of conducting samples, analyzer and sample are electrically connected resulting in an adaptation of the Fermi levels. The emitted electrons are then accelerated resp. decelerated for the difference  $|\varphi_S - \varphi_A|$  on their way to the analyzer. For this, the analyzer work function can be obtained by determining the maximum kinetic energy given by position of the Fermi edge in a spectrum.

Photoemission methods are differentiated by the choice of excitation energy. For UPS, usually energies between 0 – 100 eV are utilized to probe the valence band and thus

high lying orbitals participating in the chemical bonding. To generate such radiation in the near-ultraviolet regime, gas discharge lamps are used<sup>99</sup>, typically helium with emission lines at 21.2 eV (He I) and 40.8 eV (He II). UPS can also be performed at synchrotron beamlines with tunable photon energies below 100 eV. When X-rays serve as excitation source, one differentiates between soft and hard X-rays, the first ranging from 100 - 2000 eV and the latter exhibiting energies higher than 2000 eV, which is suited for probing deep lying core electrons of heavier elements and generally deeper layers of the sample (see further down for the dependence of information depth on X-ray energy).<sup>99-100</sup> X-rays can be produced either from conventional laboratory sources (e.g., Al  $K_{\alpha}$ ,  $h\nu = 1486.6$  eV and Mg  $K_{\alpha}$ ,  $h\nu = 1253.6$  eV) or from synchrotron sources (see Chapter 2.1). Besides the natural line width of the excitation radiation, the line width of measured photoemission peaks is determined by the analyzer resolution and the inherent natural line width of the probed state, which depends on the lifetime of the core hole according to the uncertainty principle.<sup>98</sup>

In Figure 2.2, the basic photoemission processes are schematically depicted. For XPS and UPS, photons are absorbed and electrons either from core levels (XPS) or from the valence band (UPS) are analyzed depending on their kinetic energy according to Equation (3) resp. (4). The remaining core holes will undergo one of two possible decay routes that govern their lifetime mentioned above. Generally, core holes of photoelectrons with low binding energy show Auger decay. Specifically, for excitation of the 1s core level, atoms with atomic numbers up to  $\sim 30$  mostly show Auger decay. Here, an electron of a higher lying shell fills the core hole and the released energy from this process excites another electron of the same or higher shell. The released energy must be larger than the binding energy of the excited electron for emission into vacuum. When the core hole and an electron originate from the same shell one speaks of a Coster-Kronig-transition and in case of all three electrons being located in one shell a super Coster-Kronig-transition is observed. The Auger decay is exploited in an own spectroscopic method named Auger electron spectroscopy (AES), see Figure 2.2. Core holes of photoelectrons with high binding energy or larger atoms in case of  $K$ -shell excitation will primarily follow another decay channel, which is the emission of X-ray fluorescence without any further excitation of electrons. The corresponding spectroscopic method is called X-ray fluorescence (XRF) and

is mostly used for analysis of the chemical composition of a material, as the energy of the emitted X-rays is element-specific.

In addition to the fact that the obtained binding energies from an XP spectrum are element-specific, which makes it a great tool for analysis of chemical composition (it is also a quantitative technique (see further down)), XPS is sensitive to the chemical surrounding of an atom. This phenomenon is called chemical shift and arises due to an influence of the valence

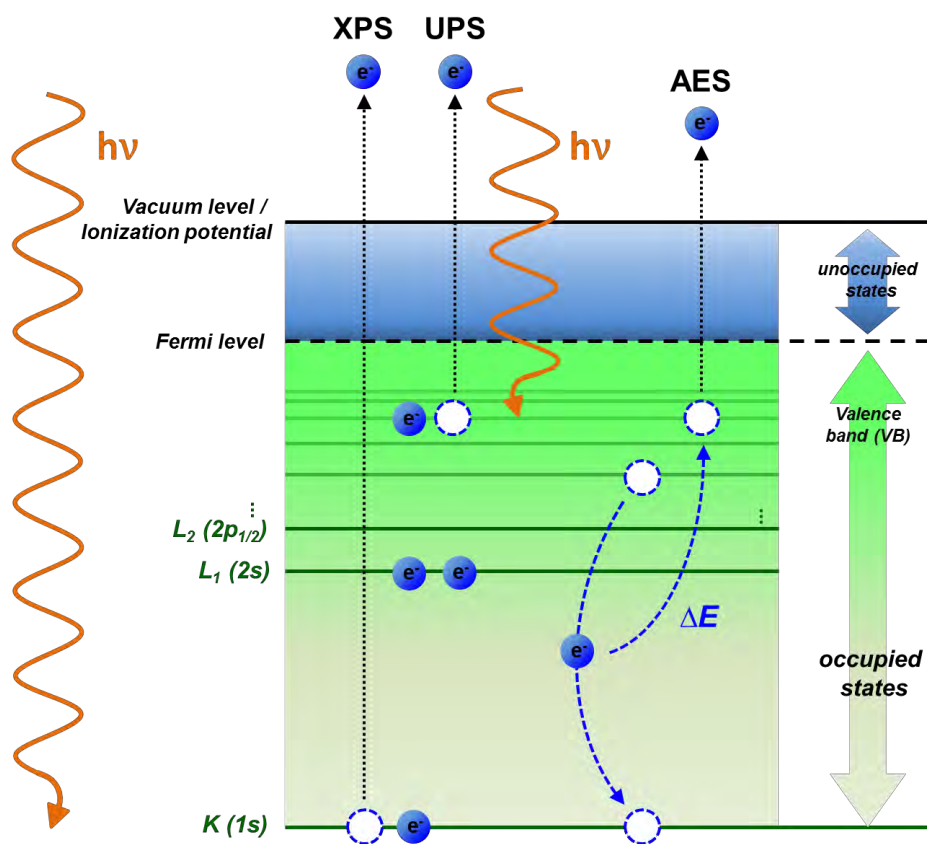


**Figure 2.2:** Left: Schematic illustration of the photoemission process for XPS and UPS. Photons are absorbed and bound core level electrons (XPS) or valence band electrons (UPS) are emitted with a kinetic energy according to energy conservation (see equation (3)). Right: Schematic illustration of the Auger decay process. A core hole is filled by an electron of a higher shell and the released energy is transferred to an electron of the same or higher shell to be emitted according to energy conservation.

electron distribution on the core electrons. Here, a superposition of initial state and final state effects governs the exact binding energy of a core electron. More generally spoken, the binding

energy  $E_B$  is the energy difference of the  $N$  electron neutral state prior to photoionization (initial state) and the  $N-1$  electron ionic state after ionization (final state)<sup>100-101</sup>

$$E_B = E_f^{N-1} - E_i^N. \quad (5)$$

Initial state effects reflect the bonding situation in a molecule in its ground state before photoexcitation. Oxidation state, neighborhood to electronegative chemical groups or bonding geometry of a molecule can influence this state and thus the electron density at the nucleus of the probed electron. The observed shifts in an XP spectrum may be relatively large, up to several electron volts are found, e.g., when comparing Pt(0) with  $E_{Pt\ 4f_{7/2}} \sim 71.1$  eV over Pt(II) with  $E_{Pt\ 4f_{7/2}} \sim 72.2$  eV to Pt(IV) with  $E_{Pt\ 4f_{7/2}} \sim 74.4$  eV.<sup>102</sup> Thus, as a rule of thumb, one observes that the binding energy increases, the stronger the electrons are bound or the more electron deficient the nucleus of the emitted photoelectron is. This effect is especially prominent for species in the gas phase where the photoelectron has to overcome the pure positive potential of the nucleus accompanied by a smaller shielding from neighboring species.

Equation (5) can be treated via the frozen-orbital approximation or Koopman's theorem, which states that after photoionization the remaining bound electrons do not change in orbital energy. By doing so, the measured binding energy approximately corresponds the negative Hartree-Fock orbital energy which can be calculated relatively easy.<sup>100</sup> In reality, final state effects lead to a lowering of the total energy of the system as the  $N-1$  electrons relax during the photoemission process.<sup>98,100-101</sup> Besides intramolecular also intermolecular relaxation effects like polarization screening and charge transfer screening from neighboring molecules or the substrate can occur. Other final state effects are shake up and shake off processes when the photoelectron either inelastically excites another electron into an unoccupied or even unbound state, respectively. Those photoelectrons are detected as satellite lines in the XP spectrum at higher binding energy. Moreover, multiplet splitting for molecules with unpaired spins, and in solids electron-hole pair and plasmon excitation is possible. One particular final state effect is the excitation of vibrational modes in molecules leading to a loss of energy of a photoelectron, e.g., vibrational excitation of a C-H bond in hydrocarbons.<sup>100-101</sup> Here, characteristic satellite peaks relative to the adiabatic main photoelectron feature are observed in terms of energy shift and intensity ratios.

---

UPS especially provides information of adsorbate structures and their geometry by characteristic positions of peaks.<sup>103-104</sup> Compared to gas phase data, adsorbates typically show broadened peaks due to interaction with the substrate. Moreover, relaxation shifts of all bands to lower binding energies are observed for adsorbed molecules due to the already discussed screening of the valence band holes by electrons of the substrates and neighboring molecules. However, differential bonding shifts to higher binding energies arise from molecular orbitals that undergo a chemical bond with the substrate. Here, for hydrocarbons typically  $\pi$  orbitals are involved.

XPS is not only a powerful tool for qualitative analysis but as inherently quantitative method it provides concentration of elements, because the number of probed atoms is directly proportional to the measured intensity. Furthermore, the probed core levels are not influenced by chemical bonding in contrast to UPS. According to Briggs and Seah, the intensity  $I_A$  of element  $A$  is given by<sup>98</sup>

$$I_A = \sigma_A(h\nu) D(E_A) \int_{\gamma=0}^{\pi} \int_{\Phi=0}^{2\pi} L_A(\gamma) \int_{y=-\infty}^{\infty} \int_{x=-\infty}^{\infty} J_0(x, y) \sec \delta T(x, y, \gamma, \Phi, E_A) \times \int_{z=0}^{\infty} N_A(x, y, z) e^{\frac{-z}{\lambda_M(E_A) \cos \nu}} dx dy dz d\gamma d\Phi \quad (6)$$

where

$\sigma_A(h\nu)$  is the cross-section for emission of a photoelectron from the relevant inner shell per atom  $A$  by a photon of energy  $h\nu$ ,

$D(E_A)$  is the detection efficiency for each electron with a kinetic energy  $E_A$  transmitted by the electron analyzer,

$L_A(\gamma)$  is the angular asymmetry of the intensity of the photoemission from atom  $A$ ,  $\gamma$  is the angle between the direction of the impinging photon and the analyzer entrance slit normal,

$J_0(x, y)$  is the photon flux per unit area at point  $(x, y)$  on the sample,

- $\delta$  is the angle between the direction of the impinging photon and the surface normal,
- $T(x,y,\gamma,\Phi,E_A)$  is the analyzer transmission function,  $\Phi$  is the solid angle,
- $N_A$  is the atom density of atoms  $A$  at  $(x,y,z)$  position,
- $\lambda_M(E_A)$  is the inelastic mean free path of electrons with kinetic energy  $E_A$  in a matrix  $M$ ,
- $u$  is the angle between surface normal and the analyzer entrance slit normal.

Equation (6) is not trivial as many of the parameters are hard to determine. Thus, in practice, one uses reference samples with exactly known concentrations/coverages of a certain species for calibration. However, if photoelectron diffraction (PED) occurs, further considerations to maintain the quantitative nature have to be done. PED is the phenomenon of the primary photoelectron wave interfering coherently with scattered electron waves as a function of emission angle and kinetic energy of the primary electron.<sup>100,105-106</sup> Such an effect can lead to deviations of the measured intensity.

As already mentioned before, UPS is non-quantitative as probed molecular orbitals generally exhibit different cross sections. It is thus not possible to compare intensities of adsorbates even if they share the same atoms. Only for identical adsorbates measured under identical conditions an intrinsic relative quantification might be possible; in case of knowing the absolute adsorbate coverage from other techniques also an absolute quantification is justified in such a special case.

Due to the nature of electron-matter interaction, XPS and UPS are both extremely surface sensitive techniques. The emitted photoelectrons obey Lambert-Beer's law where their transmitted intensity  $I$  after traveling from deeper layers into vacuum is given by

$$I = I_0 e^{-\frac{d}{\lambda_M(E_{kin})}} \quad (7)$$

where  $I_0$  is the intensity of the electrons after being created,  $d$  the escape depth and  $\lambda_M(E_{kin})$  the inelastic mean free path of the electrons with kinetic energy  $E_{kin}$  in a matrix  $M$ . The inelastic mean free path has been investigated by Seah and Dench who found a characteristic dependence of  $\lambda_M$  on the kinetic energy of the photoelectrons.<sup>98,107</sup> In Figure 2.3, this dependence is shown as

plot of  $\lambda_M$  (in units of monolayers) versus the kinetic energy for various elements. It becomes obvious that for very low kinetic energies ( $< \sim 10$  eV),  $\lambda_M$  adapts large values and at high kinetic energies beyond  $\sim 1000$  eV,  $\lambda_M$  also increases towards larger values. Only at kinetic energies between  $\sim 50$ - $150$  eV,  $\lambda_M$  crosses a minimum which implies that the surface sensitivity is maximum and only the first few atomic layers are probed. Thus, when analyzing surface properties, photoemission is performed at conditions to reach electron kinetic energies of  $\sim 100$  eV. This can only be achieved at a synchrotron, where the excitation energy can be varied (see Chapter 2.1). Another possibility to tune the surface sensitivity resp. the escape depth, is to

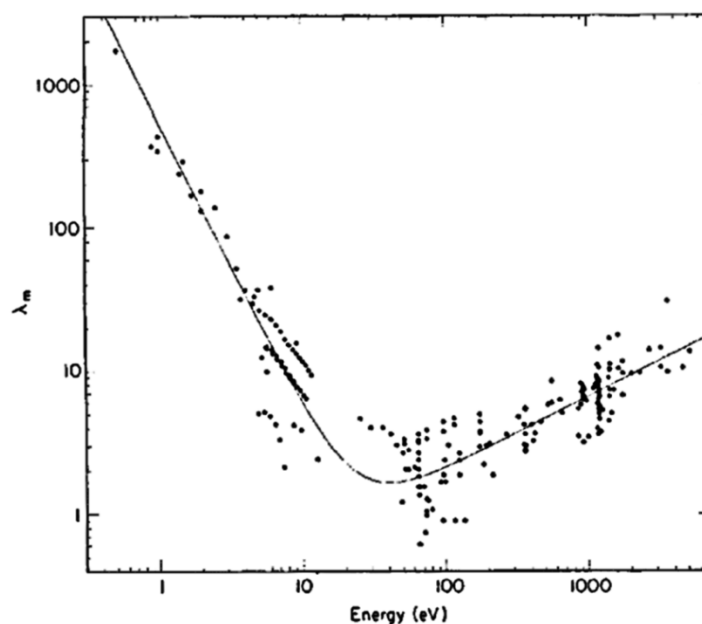


**Figure 2.3:** Logarithmic plot of the electron inelastic mean free path  $\lambda_M$  (in units of monolayers) versus kinetic energy of photoelectrons for various elements. For kinetic energies between  $\sim 50$ - $150$  eV,  $\lambda_M$  becomes minimum which means surface sensitivity is maximum. The graph is adapted from Seah et al.<sup>107</sup>

change the electron emission angle either by tilting the sample or changing the position of the analyzer. The latter approach is used in dual analyzer systems for investigating the surface or interface orientation of large molecules, especially in liquid samples when tilting is no option.<sup>108</sup> For an emission angle  $\nu$  (angle between surface normal and detector entrance slit normal) the escape depth  $d$  decreases by  $\cos(\nu)$ .

All XPS data in this thesis were collected at a synchrotron where the kinetic energy was

tuned to  $\sim 100$  eV for maximum surface sensitivity. UPS data were acquired with a helium discharge lamp. The emission angle was set to  $0^\circ$  with respect to the surface normal, for both XPS and UPS. For XPS, overall resolutions in the C 1s region were typically in the range from 150 to 220 meV and slightly higher for other core levels. The stepwise increasing background within the XP spectra arising due to inelastic losses of photoelectrons, was treated with a linear background subtraction. For UPS, no background was subtracted. For detailed information on other background models, e.g., the models of Shirley and Tougaard, see Ref.<sup>98</sup> XP spectrum deconvolution, so-called fitting, was performed using a convolution of Gaussian and Doniach-Šunjić<sup>109</sup> function to account for the asymmetry of the peaks occurring for metallic samples. Further details on background treatment and peak fitting can be found in the Ph. D. thesis of M. Kinne.<sup>110</sup>

### 2.3 Near edge X-ray absorption fine structure (NEXAFS)

Another powerful method in material and especially surface science is NEXAFS (near edge X-ray absorption fine structure). The technique is based on the absorption of X-rays by matter where the linear absorption coefficient  $\mu$  is proportional to several parameters:

$$\mu \sim \frac{\rho Z^4}{E^3} \quad (8)$$

where  $\rho$  is the sample density,  $Z$  the atomic number and  $E$  the photon energy. When performed in transmission detection mode, the transmitted intensity obeys Lambert-Beer's law with the sample thickness and the linear absorption coefficient in the exponent. For this thesis, however, partial electron yield detection mode was applied; see later for details on the different detection modes.

The basic principle of the NEXAFS method is shown in Figure 2.4. In this thesis, resonant excitation from the first core level, the  $K$ -shell, to states below or above the ionization potential is performed. A photon is absorbed whose energy resonantly excites such a core electron into an unoccupied state. Thus, NEXAFS probes the density of unoccupied states in an adsorbate. Here, excitation into unoccupied  $\pi^*$ -orbitals or above lying Rydberg states, which converge to the ionization potential, occurs.<sup>111</sup> Those transitions appear as sharp bands in the

NEXFAS spectrum slightly after the absorption edge, prior to which the excitation energy is too low to excite a transition. Resonant absorption into states above the ionization potential, so-called continuum states that are trapped in the centrifugal potential, correspond to  $\sigma^*$ -orbitals of molecules. Such transitions are observed as broad features in the spectrum. Obviously, to capture all those resonances, synchrotron radiation with tunable photon energy is needed. The created core holes will undergo either Auger or fluorescence decay, and both channels can be used for detection. Depending on the width of the region that is investigated beyond the absorption edge, one talks about NEXAFS or XANES (X-ray absorption fine structure) (up to  $\sim 50$  eV after the edge), or EXAFS (extended X-ray absorption fine structure) and SEXAFS on surfaces (surface extended X-ray absorption fine structure) (beyond  $\sim 50$  eV after the edge).<sup>93,111</sup>

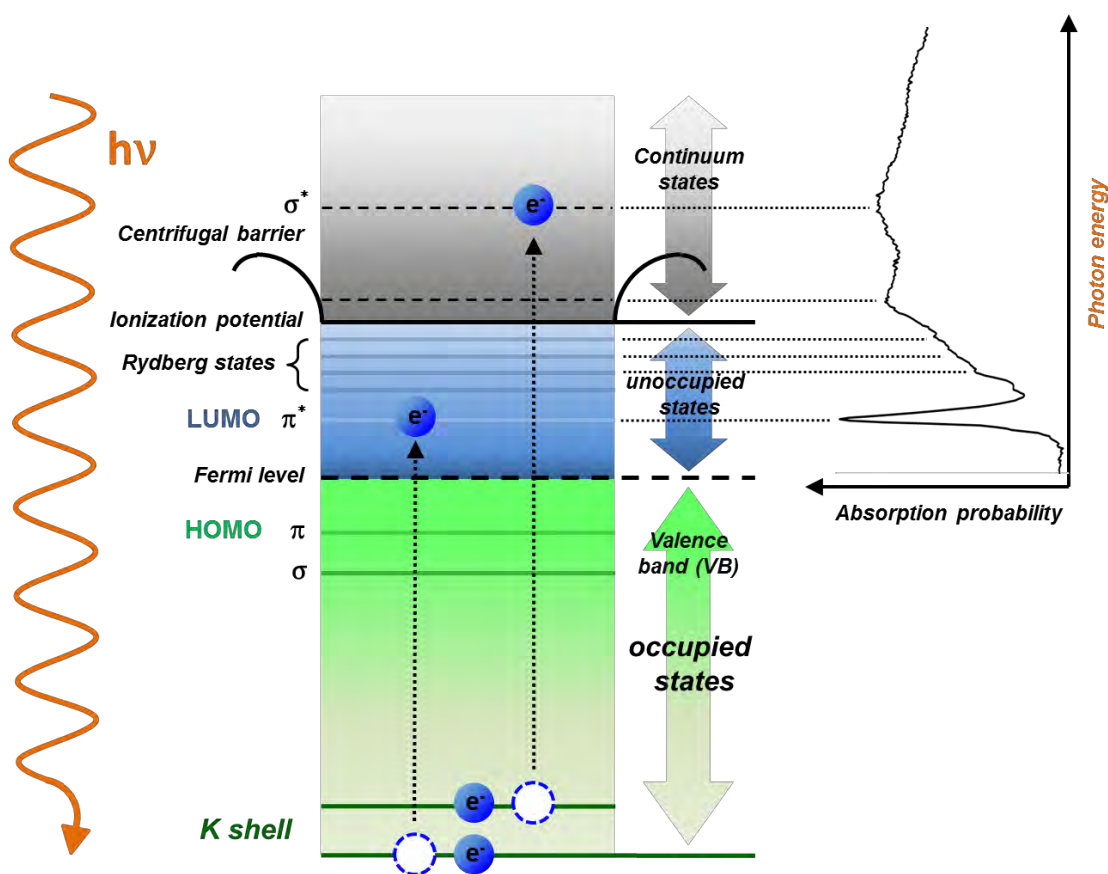


**Figure 2.4:** Schematic illustration of the X-ray absorption and generation of a NEXAFS spectrum. Core electrons are excited into unbound states above the Fermi level and simultaneously the absorption probability is detected (e.g., as current of the subsequent decay processes) as a function of photon energy.

For NEXAFS, selection rules, that can be utilized to determine the orientation of molecules on the surface, are applied. At this point, it is important to note that linearly or elliptically polarized light from a synchrotron is needed to perform NEXAFS. Often, the molecular orientation can be determined quite accurately by measuring only two spectra in extreme sample orientations, one in grazing ( $\geq 70^\circ$ ) and the other one in normal photon incidence angle ( $0^\circ$ ). If an adsorbate features  $\pi$  orbitals, in many cases it can be easily seen from the relative intensity change of the  $\pi^*$  (and also the  $\sigma^*$ ) bands if the molecule lies flat or tilted on the surface. According to the selection rules, only excitations for which the orbitals oriented parallel to the field vector of the incoming light are allowed and vice versa. When accomplishing a full analysis, i.e. measuring at various angles, an accurate orientation of adsorbates can be gained. For further details see the chapter in the book of Stöhr.<sup>111</sup> Moreover, NEXAFS is sensitive to the chemical surrounding of the probed electron, meaning it exhibits a chemical shift similar to XPS. Thus, resonance energies are sensitive to initial and final state effects, and allow for a differentiation between species of the same element.

As mentioned before, NEXAFS can be conducted in different detection modes. Besides the transmission mode (not discussed here), the fluorescence decay can be measured by a photo detector. The fluorescence yield (FY) mode has a lower surface sensitivity due to the large inelastic mean free path of photons in matter ( $\sim 10^3 \lambda_e$ ). Generally, FY exhibits lower signal-to-noise ratios than electron yield. However, the signal-to-background ratio is better in some cases for FY. For adsorbate coverages below a monolayer, typically all modes share a similar signal-to-background ratio, thus the electron yield mode becomes dominant for surface science experiments. Electron yield can be split in three types: total electron yield (TEY), partial electron yield (PEY) and Auger electron yield (AEY). The first one detects all electrons emitted from the sample including primary photoelectrons, Auger and all other secondary electrons. In case of PEY, only electrons with a certain minimum kinetic energy are detected, because an additional retarding voltage is applied. The biggest advantage of PEY is its large signal-to-noise ratio. When only electrons within a certain kinetic energy window are collected, in particular electrons from one Auger transition, AEY is applied. Due to the superior count rate of PEY over AEY and FY, in most cases it is preferred but, e.g., for very small coverages AEY can provide better results. All in all, the choice of

detection mode very much depends on the investigated system and the scientific questioning.<sup>111</sup>

A last point concerns the normalization procedure of NEXFAS spectra. As the measured intensity directly depends on the incident X-ray intensity of the beamline, which fluctuates as a function of time and photon energy, one needs a reference. Moreover, the background signal from the substrate is also undesired when measuring monolayer adsorbate structures of molecules. Reference spectra can either be acquired from a reference monitor, typically a freshly Au-coated grid, or from the clean substrate. Afterwards, either division by or subtraction of the reference signal is applied. Both methods have pros and cons depending on the scientific issue similar to the detection mode.

### 2.4 Temperature-programmed desorption (TPD)

Temperature-programmed desorption (TPD) or also referred to as thermal desorption spectroscopy (TDS) is a powerful tool widely used in surface science and catalysis. The basic setup for measuring TPD spectra consists of a sample in a UHV chamber and a quadrupole mass spectrometer (QMS). While the sample is heated with a linear heating ramp, the number of thermally induced desorbing atoms or molecules from the surface in the gas phase is monitored by QMS. If readsorption may be ignored due to sufficiently high pumping speeds, the rate  $r$  of desorption is given by an Arrhenius-type equation:<sup>112-113</sup>

$$r = -\frac{d\theta}{dt} = k_{des}\theta^n = \nu(\theta)\theta^n e^{-\frac{E_{des}(\theta)}{RT}} \quad (9)$$

$$(T = T_0 + \beta t)$$

with  $\theta$  being the coverage in monolayers,  $t$  the time,  $k_{des}$  the rate constant,  $n$  the order of desorption,  $\nu$  the pre-exponential factor,  $E_{des}$  the activation energy of desorption,  $T$  the temperature and  $\beta$  the heating rate. Due to attractive and repulsive interactions between adsorbed molecules, the parameters  $\nu$  and  $E_{des}$  are coverage-dependent. Concerning desorption order  $n$ , four different sample scenarios are possible. Zeroth-order kinetics are observed for multilayer

phases, or when a 2D gas is in very fast exchange and equilibrium with a 2D fluid or solid, as long as 2D islands are left. The desorption rate does not depend on the coverage in that cases. Desorption orders of 0.5 are found when the desorption is proportional to the circumference of islands.<sup>112,114</sup> For  $n = 1$ , molecular or atomic desorption of the adsorbed species is found and for  $n = 2$ , associative desorption takes place where two species first have to meet on the surface via diffusion processes in order to desorb. The latter case is typically found for dissociative adsorption resp. associative desorption of diatomic gases like  $H_2$ ,  $O_2$  or  $N_2$  on metal surfaces.

Analysis of TPD data is not trivial when a complete and correct evaluation according to equation (9) is desired. In short, one needs to acquire many TPD spectra with different coverages and integrate them. For every single coverage an Arrhenius plot of  $\ln r$  (or  $\theta$ ) vs.  $1/T$  has to be made delivering coverage dependent values for  $E_{des}(\theta)$  and  $\nu(\theta)$ . A less complex approach is the so-called leading edge analysis.<sup>115</sup> Here, it is assumed that within a small temperature interval at the low temperature onset of a TPD peak, the changes in overall coverage  $\theta_0$  and temperature are small. An Arrhenius plot of this short interval then provides  $E_{des}(\theta)$  and  $\nu(\theta)$ . The most frequently used but also most approximative approach is the analysis by Redhead, which gives a very fast and rough estimation of desorption energies from a single TPD spectrum by the formula<sup>116</sup>

$$E_{des}(\theta) = RT_{max} \left[ \ln \left( \frac{\nu T_{max}}{\beta} \right) - 3.46 \right] \quad (10)$$

with  $R$  being the universal gas constant and  $T_{max}$  the temperature at which the TPD peak exhibits its rate maximum. The main problem of this method lies in the initial guess of the pre-exponential factor  $\nu$  and that the desorption should be first-order for obtaining reliable results. Typically, a value of  $10^{13} \text{ s}^{-1}$  independent on coverage is chosen for  $\nu$ , but, as can be seen from equation (10), a slightly different value may change the result of  $E_{des}(\theta)$  dramatically.



## 3 Experimental setup

### 3.1 Synchrotron UHV setup

The mostly used apparatus for this thesis is the UHV ‘synchrotron machine’, depicted in Figure 3.1 and described in detail by M. Kinne.<sup>110</sup> It can be operated in the laboratory with an X-ray source or connected to a beamline at a synchrotron facility. Thus, many of the data have been acquired at beamline U49/2 PGM 1 and 2, and U56/2 PGM 2 of BESSY II, Helmholtz-Zentrum Berlin. To achieve and maintain UHV conditions down to a base pressure of  $10^{-11}$  mbar, several turbo molecular pumps, ion getter pumps, titan sublimation pumps and rotary vane pumps are

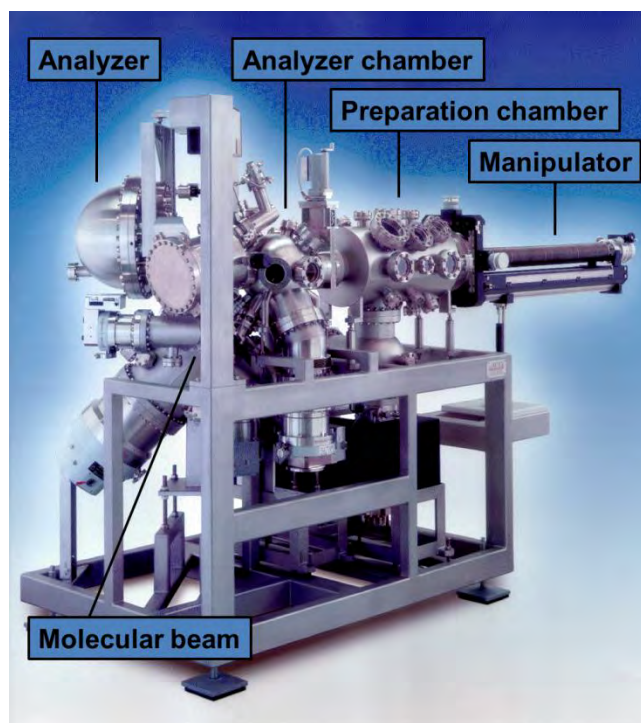


**Figure 3.1:** Picture of the synchrotron UHV setup. The main parts are highlighted.

used. The machine consists of 4 main parts: an analyzer chamber, the preparation chamber, a manipulator and supersonic molecular beam setup. In the analyzer chamber, the tools for spectroscopic measurements are housed: the hemispherical electron analyzer (Omicron EA 125 HR U7), the connections for an X-ray source and the beamline, a quadrupole mass spectrometer (Pfeiffer Vacuum Prisma QME200), a microcapillary doser and the connection to the supersonic

### 3 Experimental setup

---

molecular beam. With the quadrupole mass spectrometer, the residual gas and background gas composition during dosing experiments can be followed. The preparation chamber, separated from the analyzer chamber, is equipped with a sputter gun used for sample cleaning, electron beam evaporators used for metal evaporation, a quartz crystal microbalance for determining metal deposition rates, a LEED optics and a microcapillary doser. In order to move the sample between the two chambers and to adjust sample positions with respect to all tools, the manipulator enables precise movements in xyz spatial direction, turning for  $360^\circ$  around its axis and tilting the sample between  $0^\circ$  and  $90^\circ$ . Cooling the sample is possible with liquid nitrogen down to 100 K. Heating is performed either resistively up to 1400 K or via a filament located at the back of the sample up to 600 K. This filament prevents a change of the electron trajectory to the analyzer as no external disturbing magnetic field is established in contrast to resistive heating of the crystal. With such a setup temperature-programmed XPS (TPXPS) experiments can be conducted.<sup>101,117</sup> The temperature of the crystal is measured with spot-welded thermocouple wires. An overview of the sample holder with all important parts is shown in Figure 3.2.

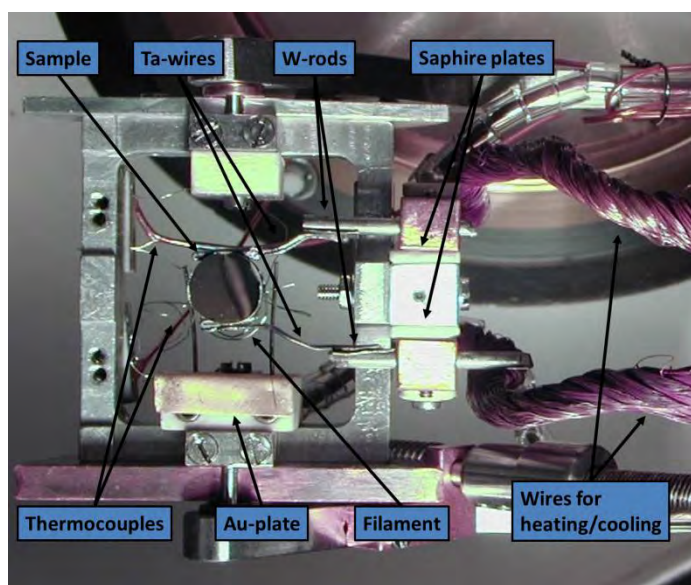


**Figure 3.2:** Picture of the sample holder. The main parts are highlighted.

The supersonic molecular beam setup allows for focusing molecular beams onto the surface while keeping the background pressure in the chamber low. In numbers this means, that local pressures of up to  $10^{-5}$  mbar hit the sample whereas the background pressure is approximately two to three orders of magnitude lower. To achieve this, a special setup of three

individually pumped stages (chambers) is necessary. The first houses the gas nozzle and a conical shaped so-called skimmer with an aperture that allows for undisturbed gas flow. Between second and third stage, a system of several apertures to bring into the beam axis is installed. Finally, a molecular beam of  $\sim 10$  mm in diameter hits the sample.

Besides using X-rays or synchrotron radiation as excitation source, it is possible to mount a gas discharge lamp at the analyzer chamber which enables measuring ultraviolet photoelectron spectra. Typically, helium is chosen with an energy of 21.2 eV for He I radiation. Another spectroscopic tool that can be used is NEXAFS. For this, a partial yield electron detector connected to an external battery box is attached to the analyzer chamber and tunable potentials are applied in order to collect the emitted electrons and measure the current within a certain energy range. A detailed description of the setup and how to operate it is given in the Ph.D. thesis of C. Gleichweit.<sup>118</sup>

## 3.2 TPD UHV Setup

In publication [P5] TPD results are presented. Those data have been measured with a TPD UHV machine described in detail elsewhere.<sup>119-120</sup> Briefly, it consists of one chamber that houses an electron analyzer, an X-ray source, a sputter gun, gas dosing facilities, a LEED optics and a quadrupole mass spectrometer (Pfeiffer Vacuum Prisma QME200) including a so-called Feulner-cup<sup>121</sup>. This instrument improves the quality and the signal-to-noise ratio of mass spectra as mostly molecules desorbing directly from the surface are detected with less disturbing signal from molecules desorbing from the backside of the crystal or sample holder and the background of the chamber.



## 4 Surface chemistry of norbornadiene/quadricyclane

As a starting point for the investigation of the NBD/QC system under UHV conditions, the Pt(111) surface is chosen, which has been proved to be very active for many surface reactions. It turned out, that Pt(111) is so reactive that the catalytically triggered conversion from QC to NBD occurs already at extremely low temperatures, which made it impossible to spectroscopically investigate this reaction with the experimental setup. However, the surface chemistry of NBD was revealed in detail by a combination of several spectroscopic methods and DFT calculations. In order to decrease the catalytic activity of the surface, platinum was exchanged for nickel, which typically is less reactive in many reactions. Indeed, besides performing the surface chemistry analysis, the conversion from QC to NBD could be followed with XPS, UPS and partly NEXAFS. Up to this point, the investigations gave basic insights into the system's behavior under UHV conditions and served as a proof of concept for the conversion. Since the parent NBD and QC compounds need to be derivatized for an efficient large scale application, dibromosubstituted analogues were investigated on the nickel surface. The choice of those compounds has mainly two reasons. First, substitution with halogens is known to red-shift the absorption maximum of NBD. Consequently, it is quite reasonable to select such compounds for investigation although they only serve as a model system since state-of-the-art NBD/QC molecular systems exhibit much larger functional groups. Secondly, an additional element in the molecule, apart from carbon, enables for measuring a second core level with XPS. As it was shown, the conversion also takes place in that system, however, the bromosubstituted compounds are unstable on the Ni(111) surface and partly lose the Br atoms already at low temperature.

### 4.1 Reaction of NBD/QC on Pt(111)<sup>[P1]</sup>

Among surface reactions, a very prominent substrate is Pt(111) on which small molecules and also larger compounds have been extensively studied.<sup>25,101,122-127</sup> For many systems, platinum shows an enhanced catalytic reactivity. Thus, it is straightforward to start the investigation of NBD/QC on Pt(111). We performed a combined experimental and theoretical study on the adsorption and thermal reaction using HR-XPS (high resolution XPS), UPS, IRAS

and DFT. To the best of our knowledge this has been the first detailed publication on surface chemistry of the NBD/QC valence isomer pair under UHV conditions.

The starting point is the adsorption of NBD and QC on the Pt(111) surface at low temperature followed with UPS. During adsorption of physisorbed multilayers for both compounds, the spectra develop several molecular peaks that allow for a facile identification of NBD and QC, see Figure 4.1a. Additionally, a comparison between the calculated density of states (DOS) for the two molecules in the gas phase with the multilayer spectra reveals a qualitative agreement when considering the differences between experiment and calculation, e.g., no final state effects such as relaxation and identical cross sections of all states for the latter. The comparison of experimental IRAS spectra of NBD and QC multilayers fits well with the corresponding calculated IR spectra from DFT. An assignment of the most intense bands in the spectral region from 600-1600  $\text{cm}^{-1}$  is performed and the characteristic vibrations are visualized using QVibePlot.<sup>128</sup> The main result for this part is the clear identification of both compounds with UPS, IRAS and DFT and moreover that QC does not convert to NBD in the multilayer regime as no spectral proof is found. Furthermore, we determined multilayer desorption around 150 K by TPXPS, TPUPS and TPIRAS.

After the investigation of physisorbed layers, sub-monolayer coverages are prepared and discussed. Again, we start with the adsorption of both compounds at low temperature using UPS as a suitable spectroscopic tool, see Figure 4.1b. The spectrum at the bottom with zero coverage corresponds to the neat Pt surface showing the 5d and 6s bands located between  $\sim 1-4$  eV. When adsorbing QC (or NBD), those Pt states get damped and simultaneously molecular features are growing, see the red QC and blue NBD spectrum on top. The molecular features Q1-Q4 are almost identical to the NBD features N1-N4 concerning relative intensity ratios and peak positions, slight binding energy shifts arise due to slightly different coverages. We thus suppose identical species being adsorbed on the surface, implying that QC is converting to NBD at a temperature  $\leq 125$  K when the molecules get in contact with the Pt surface. The same adsorption experiments are performed comprehensively with XPS as shown in Figure 4.1c. Here, we observe the evolution of two separated peaks, a main peak at 283.9 eV and a low binding energy shoulder at 283.4 eV. These peaks shift for 0.2-0.3 eV to higher binding energy due to an enhanced lateral intermolecular interaction with increasing coverage, which is attributed to an

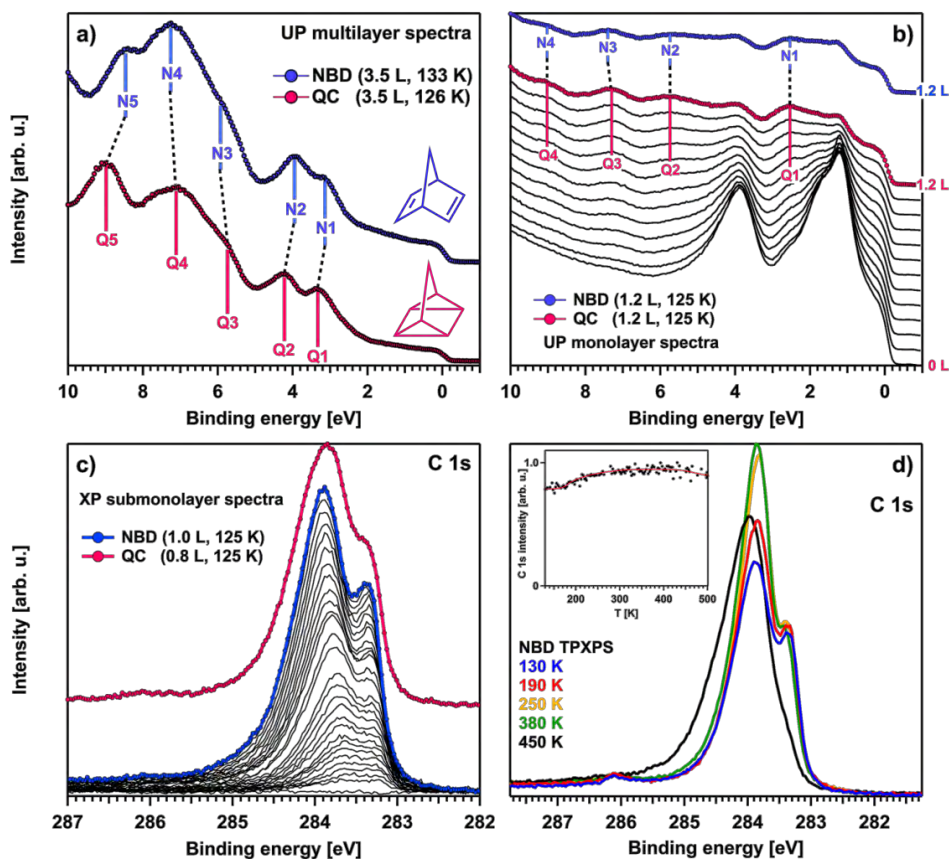


**Figure 4.1:** a) Multilayer UP spectra of NBD and QC acquired after low temperature adsorption. b) Series of QC UP spectra acquired during low temperature adsorption of a sub-monolayer. For comparison, on top a NBD spectrum at similar coverage is shown. c) Series of NBD C 1s XP spectra acquired during low temperature adsorption of a sub-monolayer. For comparison, on top a QC C 1s XP spectrum at a similar coverage is shown. d) C 1s XP spectra of NBD acquired at different temperatures during the applied linear heating ramp ( $\beta = 0.2 \text{ K s}^{-1}$ ). The inset depicts the overall intensity as a function of temperature.

initial state effect. In comparison to the red QC spectrum at a similar coverage shown on top, only a slight broadening of the spectrum is seen, e.g., the low binding energy shoulder is not as distinct for QC, probably due to hydrocarbon impurities originating from the QC synthesis. In general, the spectra of NBD and QC are identical confirming the rapid cycloreversion from QC to NBD upon contact to the surface as already found with UPS. IRAS measurements from the group of Prof. Dr. Jörg Libuda deliver analogous results, the main bands for NBD at 721 and 2690  $\text{cm}^{-1}$  occur at very similar positions of 721 and 2672  $\text{cm}^{-1}$  for QC, stating the conversion of QC. Furthermore, a conversion of QC adsorbed on a NBD-precovered surface is not observed.

The mentioned band at 2690 resp. 2672  $\text{cm}^{-1}$  is especially interesting since it reflects the bonding geometry of NBD on the surface. Hostetler et al. attributed this broad band to a softened C-H mode resulting from an interaction of the bridgehead methyl group with a Pt surface atom.<sup>59,129</sup> The donation of metal electrons from the substrate into unoccupied C-H  $\sigma^*$  orbitals causes the atypical red-shift of a C-H stretching mode to wavenumbers below 2800  $\text{cm}^{-1}$ . The group of Prof. Dr. Andreas Görling calculated IR spectra for two binding motives, one where both double bonds are in contact with the surface, called  $\eta^2:\eta^2$  geometry, and the other one with the Pt-H agostic interaction of the methyl bridgehead group and only one double bond interacting with the surface, called  $\eta^2:\eta^1$  geometry. Both geometries and corresponding calculated IR spectra are shown in Figure 4.2. One can see that only structure A exhibits a red-shifted C-H band at 2637  $\text{cm}^{-1}$  that fits to the observed 2690  $\text{cm}^{-1}$  in the experiment, whereas the spectrum for structure B differs drastically. A comparison with the experimental spectrum of NBD reveals a good match only with structure A proofing preferentially a  $\eta^2:\eta^1$  adsorption geometry. Within this geometry, both double bonds are still oriented parallel to the surface as deduced from missing y-polarized bands that are only found in the calculated spectrum of the free molecule according to the metal-surface selection rule.<sup>130</sup> However, the calculation of adsorption energies reveals the  $\eta^2:\eta^2$  geometry to be more stable for low coverages ( $\theta < 0.25$  ML), but this preference becomes smaller with increasing coverage. As the coverage in the experiment is higher (close to 1 ML), it is supposed that the adsorption energy of the  $\eta^2:\eta^1$  structure, which barely decreases with coverage, is larger at this point and thus the geometry is dominant in the experiment. Furthermore, coadsorption of CO is not included in the calculation. However, the

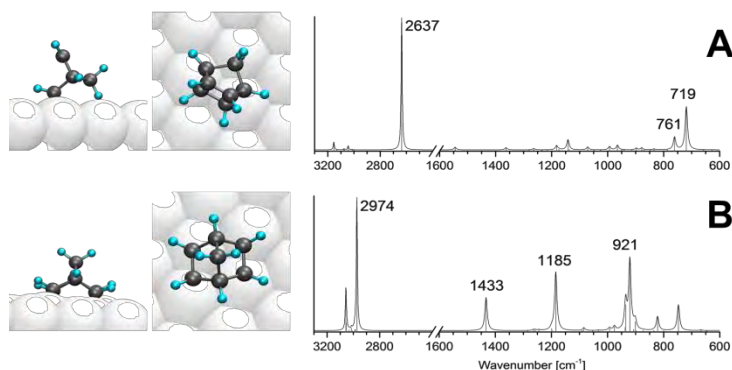


**Figure 4.2:** Possible adsorption geometries of NBD on the Pt(111) surface (side and top view) and corresponding calculated IR spectra.

experiment shows coadsorbed CO, leading to preference of the  $\eta^2:\eta^1$  orientation due to the lower space required on the surface.

Concerning the thermally induced surface chemistry of NBD, TPUPS and TPXPS experiments, supported by IRAS measurements at different temperatures, are performed using linear heating ramps of  $0.2 \text{ K s}^{-1}$ . Note that only NBD monolayers are discussed as the immediate conversion at low temperature reveals an identical behavior for QC monolayers. TPUPS data are rather uncharacteristic, mostly showing small peak shifts and intensity changes. With the help of TPXPS and TPIRAS, the reaction pathway is described, see Figure 4.3 for an overview. In Figure 4.1d, C 1s XP spectra taken during the temperature-programmed experiment are shown, starting with the blue spectrum at 130 K being identical to the last spectrum of the adsorption. At  $\sim 190 \text{ K}$  (red spectrum), the intensity of the main peak starts to rise and reaches a maximum at about 250 K (yellow spectrum). This behavior is attributed to the formation of an intermediate that exhibits different photoelectron diffraction properties as there is no other reason for the overall carbon intensity to increase, see the inset in Figure 4.1d. The intermediate is identified as a norbornadienyl species formed by dehydrogenation of NBD according to Hostetler et al.<sup>59</sup> Additionally, the almost identical spectral shape, despite the intensity change, speaks for a similar chemical structure of the intermediate and fragmentation products like benzene or ethylene can be ruled out. Norbornadienyl is stable up to  $\sim 380 \text{ K}$ , see the almost unchanged green spectrum, before a shift to higher binding energy, broadening, and vanishment of the low binding energy shoulder is observed, see light blue spectrum at 450 K. This final step is related to decomposition to  $\text{C}_x\text{H}_y$  fragments. IR spectra of NBD at 220 resp. 300 K undergo strong spectral changes compared to the situation at 160 K. The most intense bands have vanished and new characteristic peaks of the norbornadienyl intermediate have formed.

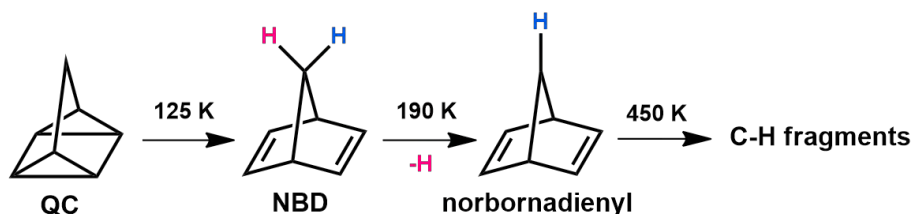


**Figure 4.3:** Overview of the thermally induced reaction pathway of QC on Pt(111).

To conclude, it seems obvious that a neat platinum surface as catalyst is too reactive to be utilized in QC activation, at least under UHV conditions. Replacing platinum with, e.g., a Ni surface, avoids a waste of rare metal as shown in the next chapter.

### 4.2 Reaction of NBD/QC on Ni(111)<sup>[P2]</sup>

As the Pt(111) surface has emerged to be too reactive in the last chapter, we switch the substrate to a non-rare and less reactive metal in order to spectroscopically observe the conversion from QC to NBD. Thus, the surface chemistry of NBD and QC on Ni(111) is investigated using UPS, HR-XPS and DFT.

In Figure 4.4a and 4.4b, UP spectra of NBD and QC during low temperature adsorption are depicted. Before dosing the molecules, the bold black spectra exhibit the 3d valence band of the Ni(111) surface. Upon exposure of NBD (QC) to the surface, the growth of 4 (6) molecular bands is observed while the valence band peaks of Ni get damped by the molecular overlayer. Those molecular features shift up to 200 meV to higher binding energy due to lateral adsorbate-adsorbate interaction. The bold blue and red spectra indicate completion of the monolayer. After highest exposure, see light blue and red spectra, the Ni 3d bands are almost completely damped and the molecular peaks have grown further in intensity. According to the very different shape between NBD and QC spectra, a clear distinction can be made, and both molecules adsorb intactly, in mono- and multilayers. When having a closer look on the binding energy shifts of the molecular features between mono- and multilayers, an upward shift is seen for all peaks except peaks 2-4 for NBD. The upward shift is caused by a lower final state relaxation in the multilayers whereas the differential downward shift of peaks 2-4 of NBD is due to a bonding and thus energy gain of the  $\pi$  orbitals of NBD with the surface.

In the next step the adsorbed monolayers for both compounds are heated with a linear heating ramp while simultaneously acquiring UP spectra in a TPUPS experiment. Here, especially the QC spectrum undergoes drastic changes when heating to about 200 K. To visualize those changes, the most characteristic peak ratios for NBD (peak 3/4) and QC (peak 5/6) are plotted versus temperature in Figure 4.4c. At about 168 K, those ratios become equal after being very different at lower temperatures. This implies that the conversion from QC to

NBD is finished at 168 K, also obvious from completely identical UP spectra at this temperature. The identical development of the ratios for  $T > 168$  K confirms that the conversion from QC to NBD has taken place.

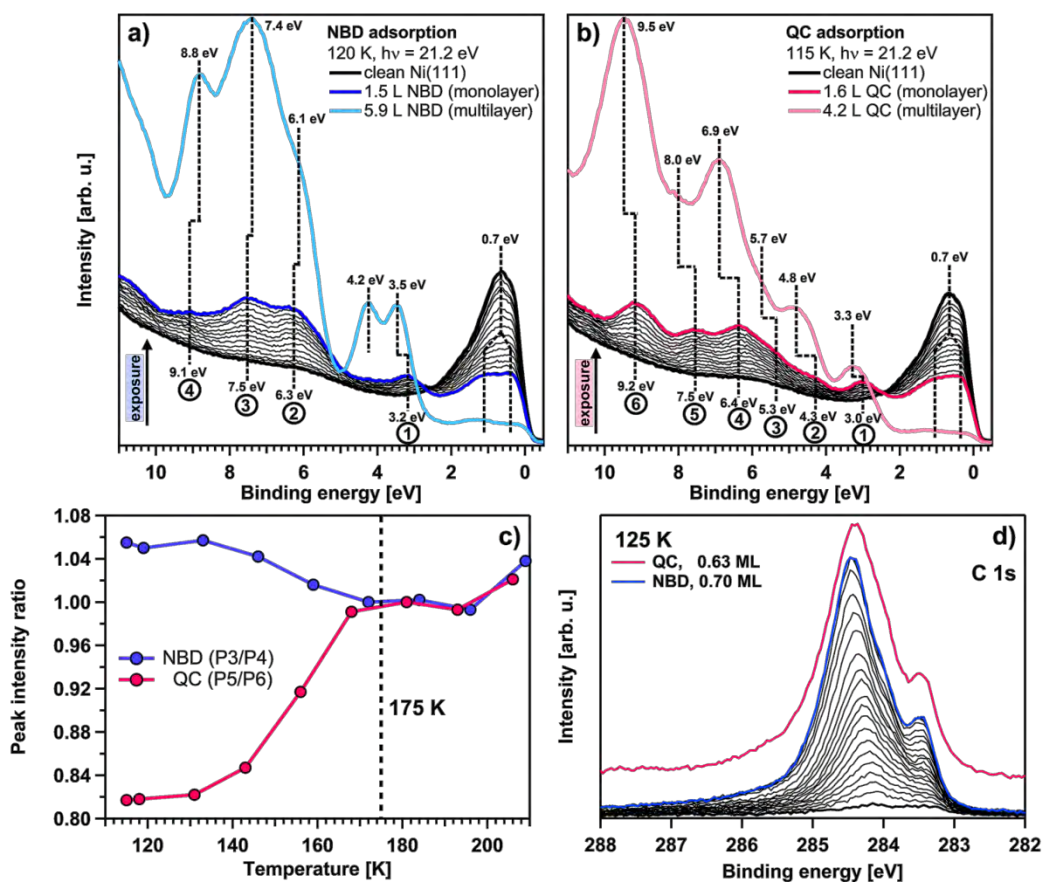


**Figure 4.4:** a) UP spectra of NBD measured during low temperature adsorption. b) UP spectra of QC measured during low temperature adsorption. c) Plot of the intensity ratio of characteristic peaks for NBD and QC versus temperature revealing the conversion temperature from QC to NBD. d) C 1s XPS spectra acquired during low temperature adsorption of NBD. For comparison, on top a QC spectrum at similar coverage is shown.

To obtain information on adsorption geometry, DFT calculations are performed by the group of Prof. Dr. Andreas Görling, similar to the Pt(111) study, including the stable  $\eta^2:\eta^2$  and  $\eta^2:\eta^1$  orientations. At low coverages, for NBD, the  $\eta^2:\eta^2$  structure is by far more stable (2.34 to 1.67 eV) whereas for QC,  $\eta^2:\eta^1$  orientation is slightly favored (0.78 to 0.71 eV). Moreover, transformation from QC to NBD as on Pt(111) is not observed within the calculation. At

monolayer coverage, for NBD, the adsorption energy is lowered by 0.6 eV for  $\eta^2:\eta^2$  and only 0.08 eV for the  $\eta^2:\eta^1$  motive due to reduced hydrogen-hydrogen van der Waals interaction of the latter. In contrast, for QC, the adsorption energy of the  $\eta^2:\eta^2$  mode increases by 0.15 eV due to a stabilization by higher significance of intermolecular van der Waals interactions as compared to the molecule-substrate bonds. The  $\eta^2:\eta^1$  geometry of QC is just lowered for 0.03 eV. Thus, QC may undergo a change in adsorption geometry at high coverage whereas NBD should maintain the  $\eta^2:\eta^2$  motive.

When looking at the XP C 1s spectra of the molecules, surprisingly we find almost identical spectra for both compounds at comparable coverage, see Figure 4.4d. The spectrum consists of three peaks (283.44, 284.09 and 284.51 eV) that shift to higher binding with increasing coverage caused by lateral molecule-molecule interactions. The peak ratio of 1:2:4 is in line with the number of equivalent carbon atoms in both molecules, at least for the  $\eta^2:\eta^2$  orientation. When closer analyzing the spectral shape of both compounds from low temperature to 180 K, the conversion of QC to NBD still can be observed with XPS, however the spectral changes are small, probably also due to a significant amount of priorly converted NBD in the QC sample.

Next, the thermal evolution of NBD measured with XPS during a linear heating ramp is discussed. Note that the QC experiment is not discussed as QC has converted to NBD before and thus the behavior is identical. In Figure 4.5a, the C 1s XP spectra at different temperatures are shown with the corresponding quantitative analysis from peak fitting in 4.5b and the summarized reaction pathway in 4.5c. Starting at about 190 K, the growth of a new low binding energy peak is observed while the main peaks broaden and shift to higher binding energy (see, e.g., red spectrum at 250 K). This is attributed to decomposition of NBD into benzene and methylidyne. At about 330 K, the low binding energy peak starts to vanish and the main feature shifts to lower binding energy while further broadening (see brown spectrum). Here, the molecule decomposes into smaller uncharacteristic  $C_xH_y$  fragments whereas at even higher temperatures, e.g., 600 K (see green spectrum), amorphous carbon and carbide are left on the surface after complete dehydrogenation.

As an additional spectroscopic technique, NEXFAS is applied to get further information of the processes and on the orientation of the molecules on the surface. At low temperature, a

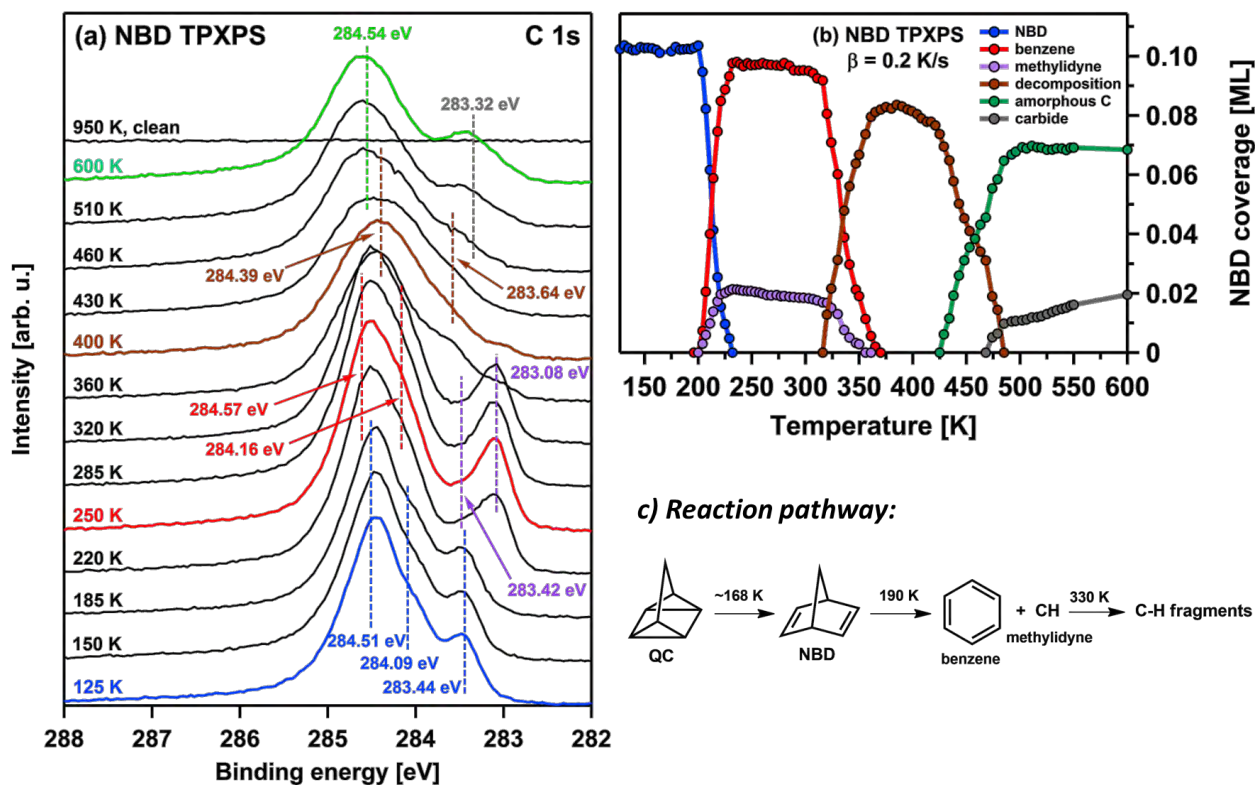


**Figure 4.5:** a) Selected C 1s XP spectra of NBD at different temperatures taken during the applied heating ramp. b) Quantitative analysis of the NBD TPXPS experiment in a). c) Overview of the thermally induced reaction pathway of QC on Ni(111).

characteristic  $\pi^*$  resonance is found for NBD only in grazing incidence, confirming the parallel orientation of the two double bonds to the surface plane. However, for QC, also  $\pi^*$  intensity is observed but to a lower degree. This is attributed to NBD impurities in the QC sample as already mentioned before. Upon heating above the conversion temperature, as expected only minor changes in the spectra appear besides an increase of the QC  $\pi^*$  intensity pointing towards the conversion of remaining QC molecules in the sample. At 250 K, when benzene and methylidyne formation occurs, a shift of the  $\pi^*$  resonance is found, that is again only visible in the grazing incidence spectra, indicating a flat lying benzene molecule. Simulated NEXAFS spectra state a  $\eta^2:\eta^2$  adsorption geometry of NBD in the monolayer coverage regime by comparison with the experimental data.

To conclude, we have shown that the catalytic thermal conversion of QC to NBD can be followed spectroscopically on Ni(111). We can clearly identify both, NBD and QC on the

surface and propose an adsorption geometry for both compounds. In general, the Ni(111) substrate is less reactive in comparison to the Pt(111) surface and moreover, reveals a different reaction pathway concerning molecule decomposition.

### 4.3 Reaction of 2,3-dibromosubstituted NBD/QC on Ni(111)<sup>[P3]</sup>

In this study the adsorption, energy release and reaction of 2,3-dibromosubstituted NBD and QC are investigated on Ni(111). These compounds serve as model for further studies with derivatized NBD/QC systems. The approach here was to choose a useful substitution pattern and also keep the molecular structure close to the parent NBD/QC system. The surface chemistry of the system was analyzed mainly using XPS supported by DFT calculations and UPS.

Starting with the low temperature (~110 K) adsorption of Br<sub>2</sub>-NBD in the C 1s core level, the formation of 4 peaks at 283.35, 283.70, 284.15 and 284.76 eV is observed, see Figure 4.6a. The peak area ratios and binding energy differences are kept constant during the fitting procedure. With increasing coverage, the peaks shift to higher binding energy for a maximum value of 120 meV due to growing lateral molecule-molecule interactions. Because of the complexity of the Br<sub>2</sub>-NBD molecule, it is not possible to assign the fitted peaks to specific carbon atoms. For Br<sub>2</sub>-QC, see Figure 4.6b, a completely different spectral shape is found during low temperature (~110 K) adsorption with 5 peaks at 283.47, 284.04, 284.43, 284.98 and 285.54 eV. The fitting parameters are also kept constant and the peaks shift to higher binding energy with increasing coverage for about 300 meV. As both spectra differ quite a lot, conversion of Br<sub>2</sub>-QC to Br<sub>2</sub>NBD is excluded at this point and molecular adsorption is supposed.

In the Br 3d core level, two species for both molecules are observed during adsorption at low temperature (~130 and 115 K), see Figure 4.6c and 4.6d. For both, the same peak at 68.98 resp. 69.00 eV is observed and for Br<sub>2</sub>-NBD resp. Br<sub>2</sub>-QC another peak at 70.27 resp. 70.31 eV is found. Due to the high binding energy difference between the two species for both compounds, 1.29 resp. 1.33 – 1.39 eV, the low binding energy feature is attributed to atomic Br from dissociation of the molecules whereas the high binding energy peak corresponds to the intact Br atoms in the molecules. This interpretation is in agreement with literature, where comparable binding energy shifts of halogen core level peaks between atomic and intact species

are found.<sup>131-133</sup> Moreover, for CH<sub>3</sub>Br on Ni(111) dissociation has been found at T < 120 K.<sup>134</sup> Concerning the very different ratios of atomic and bound Br between the two molecules, we believe that for Br<sub>2</sub>-QC the C-Br bond is more stable than the C-Br bond in Br<sub>2</sub>-NBD due to a higher stabilization of the corresponding carbocations.

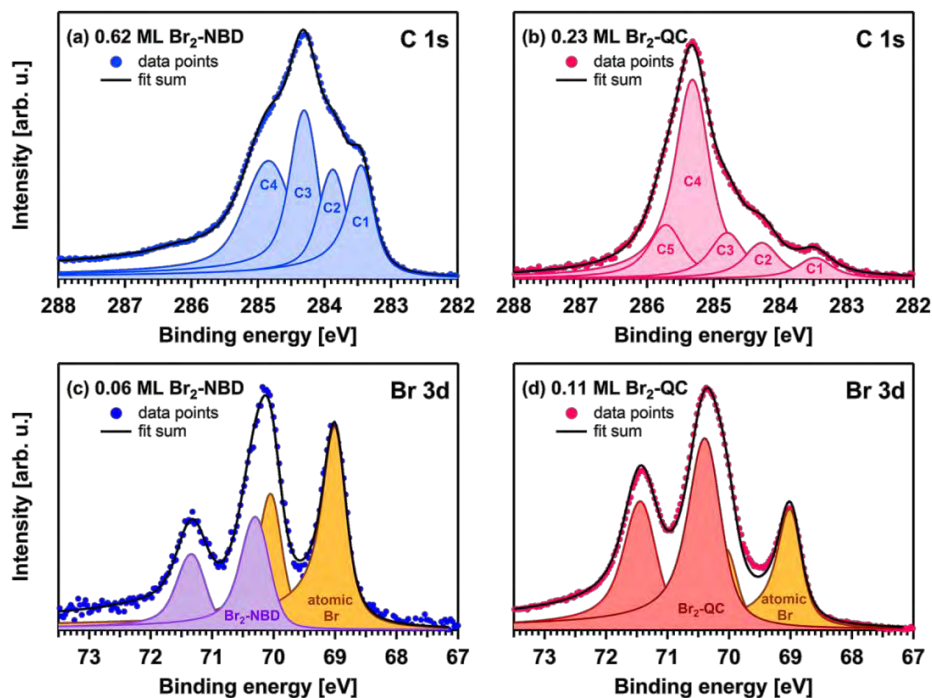


**Figure 4.6:** *C 1s* XP spectra of a) Br<sub>2</sub>-NBD and b) Br<sub>2</sub>-QC and Br 3d XP spectra of c) Br<sub>2</sub>-NBD and d) Br<sub>2</sub>-QC. The peaks obtained from the fitting procedure are highlighted.

To obtain adsorption geometries and energies, the group of Prof. Dr. Andreas Görling performed DFT calculations. Br<sub>2</sub>-NBD most favorably adsorbs in a  $\eta^2:\eta^1$  mode with the Br atoms pointing away from the surface due to repulsive interactions of Br and the Ni surface. In case of Br<sub>2</sub>-QC, also the  $\eta^2:\eta^1$  configuration is the most stable structure, however, with Br atoms not pointing away but adsorbed on on-top sites. Here, the interaction with the surface is smaller in general as the Br atoms exhibit a larger distance from the surface than in the comparable structure of Br<sub>2</sub>-NBD (which is not the most stable geometry). Thus, a stabilizing Br-Ni interaction is supposed.

Next, the thermal evolution of both molecules is investigated in both core levels by TPXPS. The corresponding quantitative analysis is shown in Figure 4.7, with the color-coded

density plots of the TPXPS experiments being depicted in Figure 4.8. Starting with  $\text{Br}_2\text{-NBD}$  measured in the C 1s core level, up to 195 K no spectral changes are observed. Afterwards, a quantitative decomposition to benzene and methylidyne, well known from the behavior of pure NBD on Ni(111), is observed. Additionally, the high binding energy shoulder (peak C4) decreases, which is attributed to the cleavage of the C-Br bonds. Note that from the start of the

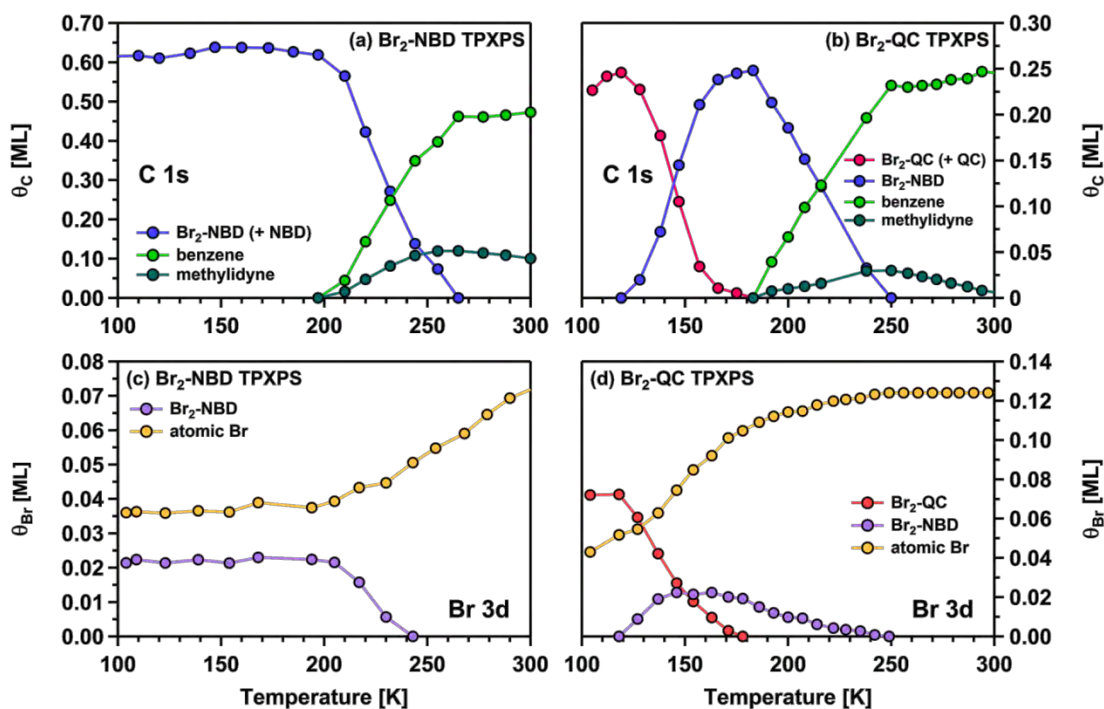


**Figure 4.7:** Quantitative analysis of the TPXPS experiments of a)  $\text{Br}_2\text{-NBD}$  and b)  $\text{Br}_2\text{-QC}$  measured in the C 1s core level and c)  $\text{Br}_2\text{-NBD}$  and d)  $\text{Br}_2\text{-QC}$  measured in the Br 3d core level.

experiment NBD is present besides  $\text{Br}_2\text{-NBD}$  according to the ratio found during the adsorption. When looking at the  $\text{Br}_2\text{-QC}$  data, a drastic spectral change is observed already starting at 130 K. All peaks (C1-C5) are vanishing and new peaks form at binding energies similar to the 4 peaks of  $\text{Br}_2\text{-NBD}$ . Here, the conversion from  $\text{Br}_2\text{-QC}$  to  $\text{Br}_2\text{-NBD}$  takes place. At  $\sim 195$  K, the same decomposition pathway to benzene and methylidyne is found. The Br 3d TPXPS experiment reveals the mentioned cleavage of the remaining C-Br bonds starting at  $\sim 195$  K up to 250 K while the signal for atomic Br is accordingly increasing. Obviously, for  $\text{Br}_2\text{-NBD}$ , the C-Br cleavage occurs simultaneously with the decomposition step to benzene and methylidyne, probably being the energetically favored situation. In the case of  $\text{Br}_2\text{-QC}$  measured in the Br 3d core level, the conversion to  $\text{Br}_2\text{-NBD}$  is also observed, starting at  $\sim 130$  K and indicated by a

shift of 40-100 meV to lower binding energy, which fits with the Br<sub>2</sub>-NBD peak. However, the amount of produced Br<sub>2</sub>-NBD is much lower than it has been observed in the C 1s data whereas the stability range is identical. At the same time, the signal for atomic Br severely grows (at 70 K lower temperature than for Br<sub>2</sub>-NBD), which implies that the C-Br bond in Br<sub>2</sub>-QC breaks simultaneously with the conversion. The C 1s data did not allow for a differentiation between intact Br<sub>2</sub>-NBD and NBD without Br, but the Br 3d core level enables to determine the fraction of intact Br<sub>2</sub>-NBD.

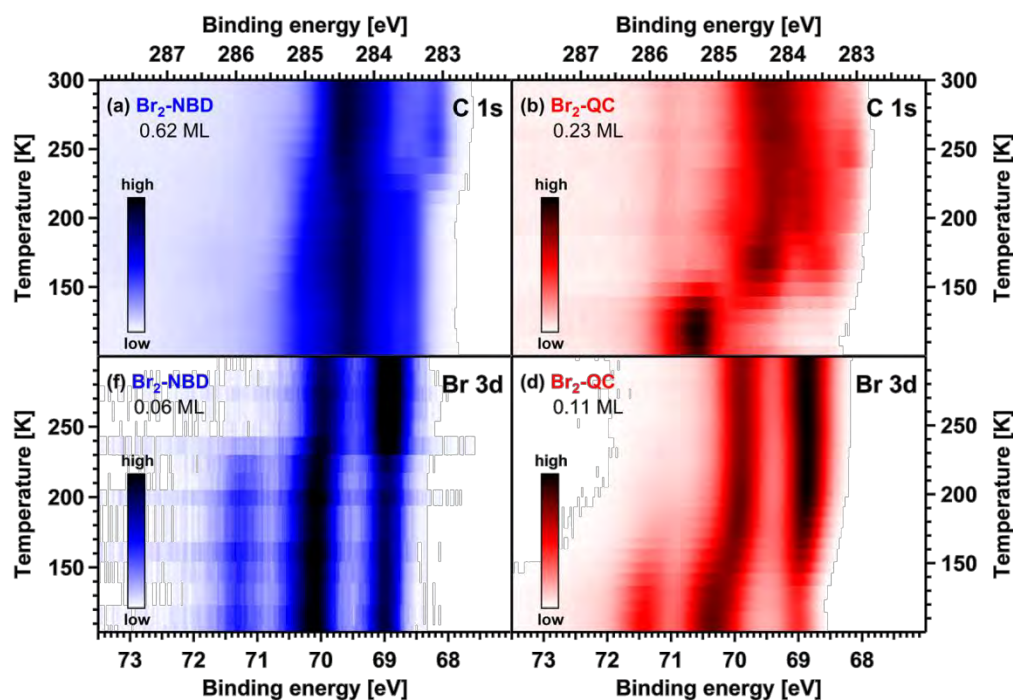


**Figure 4.8:** Color-coded density plots of the TPXPS experiments from 110 – 300 K for a) Br<sub>2</sub>-NBD (C 1s), b) Br<sub>2</sub>-QC (C 1s), c) Br<sub>2</sub>-QC (Br 3d) and d) Br<sub>2</sub>-QC (Br 3d).

Finally, we performed UPS of both compounds during the adsorption and the temperature-programmed experiment. Characteristic UP spectra are obtained from the adsorption of both molecules. However, during TPUPS, in the range of the conversion temperature the spectra of both molecules do not resemble each other at any temperature. The reason is that for Br<sub>2</sub>-NBD mainly the intact molecule is present, whereas for Br<sub>2</sub>-QC mostly NBD is forming during the conversion. Thus, the UP spectra at, e.g., 190 K cannot be identical or similar.

To conclude, the conversion of Br<sub>2</sub>-QC to Br<sub>2</sub>-NBD is observed on Ni(111) at similar

temperatures as QC conversion occurs on Ni(111). The reaction pathway to benzene and methylidyne is also identical since the C-Br bonds get cleaved before decomposition. However, the fact that large fractions of the adsorbed molecules (more in case of Br<sub>2</sub>-NBD) dissociate already at low temperature on Ni(111), classifies the dibromosubstituted system only as model study.

## 5 Catalyst modification

In this chapter two modified surfaces are investigated using typical test molecules, CO, ethylene and benzene, in order to probe their catalytic activity. The first one is a bimetallic  $\text{Pt}_x\text{Ag}_{1-x}/\text{Pt}(111)$  surface that may also serve as catalyst for NBD/QC systems analogous to pure Pt(111), which has proven to be too reactive. The bimetallic surface, however, shows interesting catalytic properties that may alter the QC reactivity in a desired way. As a second modified surface, carbide-modified Mo(110) is chosen, which is known to exhibit similar catalytic activity compared to Pt group metals for specific reactions, e.g., dehydrogenation reactions. The initial idea with this approach was to find working catalysts for LOHC dehydrogenation besides existing rare metals. Indeed, the carbide surface exhibits a high catalytic activity, even larger than Pt(111), towards the dehydrogenation of small hydrocarbons. It could also be worth to test this surface for QC conversion, however, an analysis with XPS may be difficult due to the overlapping signals of the carbide and the molecule peaks in the C 1s core level. Nevertheless, carbide-modified molybdenum surfaces provide a real alternative in catalysis.

### 5.1 Reaction of CO and $\text{C}_2\text{H}_4$ on bimetallic $\text{Pt}_x\text{Ag}_{1-x}/\text{Pt}(111)$ surface alloys<sup>[P4]</sup>

In the search for new and abundant catalysts, bimetallic systems occupy a large field. The main goal is focused on finding and characterizing systems that sustain the catalytic activities of existing catalysts or even outperform them while saving precious metal content. Here, the catalytic activity of  $\text{Pt}_x\text{Ag}_{1-x}/\text{Pt}(111)$  surfaces in comparison to neat Pt(111) are studied with CO and  $\text{C}_2\text{H}_4$  as probe molecules. For this, the adsorption and thermal reaction of both molecules is studied using HR-XPS.

The formation of  $\text{Pt}_x\text{Ag}_{1-x}/\text{Pt}(111)$  surfaces has been extensively studied: the 2D alloy is formed when annealed to  $\sim 550 - 900$  K and is restricted to the topmost layer with a tendency for phase separation.<sup>135-140</sup> Thus, and because the discussion of the preparation and characterization of the alloy has not been the main focus of this publication, it will not be addressed here. CO adsorption on the alloy has also been investigated before, however, only using vibrational

spectroscopy and TPD<sup>139-140</sup>. Consequently, only the most important results will be briefly presented.

CO is adsorbed on surface alloys with varying Ag concentration ( $\theta = 0.33, 0.50, 0.62$  and  $0.68$  ML) at low temperature while acquiring C 1s XP spectra until saturation. For all Ag coverages, the growth of two CO species is found, according to the very similar binding energy compared to CO/Pt(111) (maximum deviation is below 180 meV depending on species, Ag content, and CO coverage). One is attributed to CO on-top and the other to CO on bridge sites whereas the on-top species is more stable and populated first.<sup>122</sup> The overall CO coverage decreases linearly with Ag content, because CO adsorption on Ag facets is not favorable with a desorption temperature around 130 K<sup>139</sup> and even  $\sim 50$  K on Ag(111)<sup>141</sup>. However, the relative ratio between CO<sub>on-top</sub> and CO<sub>bridge</sub> changes, meaning both sites are not equally occupied at saturation. CO<sub>on-top</sub> becomes the dominant species at high Ag contents. Furthermore, a main difference is the observation of CO<sub>bridge</sub> for all Ag coverages, whereas in the literature this species has only been observed for  $\theta_{Ag} < 0.3$  ML with vibrational spectroscopy. The reason most probably lies in the high sensitivity of XPS to detect smallest amounts of carbon.

In the next step, a linear heating ramp is applied to the CO covered surfaces while simultaneously measuring C 1s XP spectra. The quantitative analysis reveals that no CO desorption occurs before 350 K. Above 350 K, CO<sub>bridge</sub> starts to desorb and a shift in desorption temperature of up to  $\sim 105$  K at 0.68 ML Ag content compared to CO/Pt(111) is observed. For CO<sub>on-top</sub>, desorption sets in at slightly higher temperatures, with a maximum change of desorption temperature by  $\sim 45$  K. According to this change in desorption temperatures, the adsorption energies, which are calculated using the Redhead approximation, also show a strong dependence on the Ag concentration, see Figure 5.1a. Compared to Pt(111), a large increase from 107 kJ/mol<sup>110</sup> to 148 resp. 129 kJ/mol for on-top resp. bridge sites at highest Ag content is found. Again, this result does not contradict the absence of CO<sub>bridge</sub> in the TPD measurements of Schüttler et al. as their experimental setup could not resolve the two CO species.<sup>140</sup> In general, we confirm the observation of increased CO adsorption strength due to lateral ligand effects of adjacent Ag atoms next to small Pt ensembles. However, this is not only true for CO<sub>on-top</sub> but also for CO<sub>bridge</sub>.

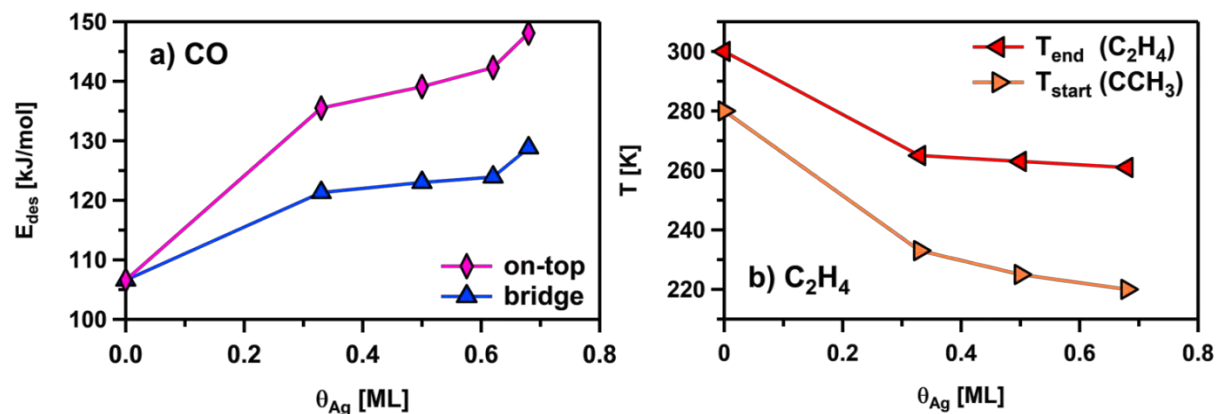


**Figure 5.1:** a) Desorption energies of  $\text{CO}_{\text{on-top}}$  and  $\text{CO}_{\text{bridge}}$  species as a function of Ag surface concentration of different  $\text{Pt}_x\text{Ag}_{1-x}/\text{Pt}(111)$  bimetallic surfaces. The energies are calculated using a Redhead approximation. b) Dependency of the stability of  $\text{C}_2\text{H}_4$  and formation of the intermediate  $\text{CCH}_3$  on Ag surface concentration of different  $\text{Pt}_x\text{Ag}_{1-x}/\text{Pt}(111)$  bimetallic surfaces.

In the second part of the publication,  $\text{C}_2\text{H}_4$  is investigated analogously to CO on different surface alloys. During low temperature adsorption on Pt(111), the C 1s spectrum exhibits three peaks: one main adiabatic feature and the first and second vibronically excited states with defined binding energy shifts and intensity ratios according to the linear coupling model.<sup>101,142-143</sup> On the alloys, the C 1s XP spectra reveal a new peak besides the main feature for  $\text{C}_2\text{H}_4$  adsorbed on Pt(111) facets. As the main feature shows a very similar binding energy compared to  $\text{C}_2\text{H}_4$  on Pt(111) (283.11 compared to 283.24 eV), we attribute this new peak to adsorption on Pt(111) facets with only minor influence of Ag atoms. The additional feature otherwise is assigned to molecules adsorbed on Pt sites that are in contact and influenced by adjacent Ag atoms/arrays, or on mixed Pt/Ag sites. The overall coverage of adsorbed molecules drops linearly with Ag content, similar to the CO case, due to the fact that ethylene does not adsorb on Ag(111) under these conditions.

To identify the reaction pathway of ethylene, a linear heating ramp is applied to the different alloys and XP spectra are measured simultaneously. Concerning the intermediates, an identical reaction pathway compared to Pt(111) is observed. On Pt(111), at  $\sim 280$  K ethylidyne ( $\text{CCH}_3$ ) is formed accompanied by a short living minor intermediate, identified as ethylidene ( $\text{CHCH}_3$ ), followed by decomposition into carbon fragments around 420 K.<sup>142-143</sup> On the alloys,

however, there are some major differences, especially lower reaction temperatures are observed. It becomes obvious that the alloys show an increased reactivity as  $\text{CCH}_3$  is formed at much lower temperatures (up to 60 K at 68% Ag content) and  $\text{C}_2\text{H}_4$  is less stable as indicated by the temperature when it has reacted, see Figure 5.1b. Another important difference is that almost 100% of adsorbed ethylene molecules decompose into ethynidyne on the alloys, whereas on Pt(111) about 40% of them are desorbing before a reaction occurs.

In conclusion, we demonstrated by CO and  $\text{C}_2\text{H}_4$  as probe molecules that the bimetallic alloy system  $\text{Pt}_x\text{Ag}_{1-x}/\text{Pt}(111)$  alters the reactivity drastically compared to a neat Pt(111) substrate. CO exhibits a stronger bonding to the surface, while  $\text{C}_2\text{H}_4$  shows an increased reactivity, meaning reactions occur at lower temperatures. This offers new possibilities in catalysis, e.g., QC cycloreversion to NBD, and also allows for precious material saving.

### 5.2 Reaction of $\text{C}_2\text{H}_4$ , $\text{C}_6\text{H}_6$ and $\text{C}_6\text{H}_{12}$ on C/Mo(110)<sup>[P5]</sup>

Another interesting catalyst group are transition metal carbides, which have attracted a lot of attention especially as dehydrogenation catalysts where they can replace Pt-group metals in reactions like hydrogenation, dehydrogenation and hydrolysis.<sup>84</sup> Among the dehydrogenation of liquid organic hydrogen carrier (LOHC) project<sup>25-26,144</sup> in our working group, mostly performed on Pt(111) as catalytic surface, we have searched for new alternative catalysts and decided to characterize and probe molybdenum carbide.

The preparation, characterization and oxidation of the carbide, and furthermore the interaction with CO as probe molecule, has been performed by Gleichweit et al.<sup>89-90</sup> As a next step, we want to invest the reaction of larger molecules of the class of hydrocarbons on monolayer C/Mo(110). For this, ethylene and benzene are chosen as probe molecules. By a combination of HR-XPS, TPD and NEXAFS, the reaction pathway of both molecules is resolved in detail.

We start discussing the adsorption of ethylene on the monolayer carbide at low temperature, see Figure 5.2a for the corresponding C 1s XP spectra. The sharp peak at 282.81 eV in the beginning arises due to the carbide. When adsorbing ethylene, two broad peaks simultaneously grow at 283.33 and 284.23 eV, and saturate with a coverage of 0.33 ML of  $\text{C}_2\text{H}_4$ .

Similar saturation values have been found on other substrates like Ni(111), Pt(111) and Ru(001).<sup>145-147</sup> During adsorption, the carbide peak shifts to higher binding energy by 70 meV, which is attributed to an adsorbate-induced core level shift. The two species for C<sub>2</sub>H<sub>4</sub> can be linked to different adsorption sites of the molecule with similar adsorption energy. Next, a TPXPS experiment is performed, see Figure 5.2b for the C 1s XP spectra and 5.2c for a color-coded density plot for better visualization. Note that the carbide peak is subtracted and difference spectra are shown. At 180 K, a new peak starts to grow on cost of the ethylene features. Up to 330 K, when the maximum intensity of the new species is reached, 23% of ethylene has desorbed, whereas the remaining molecules dehydrogenate. As the full width at half maximum is much smaller for the new species, a clear assignment to a CCH<sub>3</sub> species including vibrational fine structure is possible.<sup>101,142-143</sup> Above 330 K, CCH<sub>3</sub> decreases and a new peak forms at 283.14 eV, which is attributed to adsorbed carbon, meaning the full decomposition (dehydrogenation) of the molecule sets in. The results of the TPXPS experiment are confirmed by TPD measurements shown in Figure 5.3a. We find two peaks in the TPD spectra of ethylene on the carbide at 300 and 396 K. Interestingly, no coverage-dependent shift of both peaks is observed, in contrast to H<sub>2</sub>/C/Mo(110) and as would be expected in case of associative desorption of hydrogen. However, here a desorption order of 1 is supposed since adsorption sites are missing for the evolved hydrogen and thus immediate desorption is proposed. Deconvolution of the TPD spectra reveals a peak area ratio of 1:3, in perfect agreement with the reaction pathway, where at first one H atom gets abstracted when ethylidyne is formed and subsequently the remaining three H atoms get released by complete dehydrogenation to carbon. Finally, NEXAFS measurements in normal and grazing incidence angle position reveal a non-flat adsorption geometry for ethylene, as in both angles  $\pi^*$  intensity is found. This is in agreement with the observation of two carbon species during the adsorption, probably related to ethylene adsorbed on different sites.

The second probe molecule to be investigated on the monolayer carbide is benzene. Starting with the adsorption at low temperature, as depicted in Figure 5.2d, two species are developing at 283.97 and 284.47 eV in the C 1s XP spectra. Similar to C<sub>2</sub>H<sub>4</sub>, the two species are either attributed to intramolecular different sites for the carbon atoms or to adsorption of C<sub>6</sub>H<sub>6</sub> on different adsorption sites. To reveal the thermal reaction pathway on the surface, again a linear heating ramp is applied, see Figure 5.2e for the corresponding spectra and 5.2f for the color-

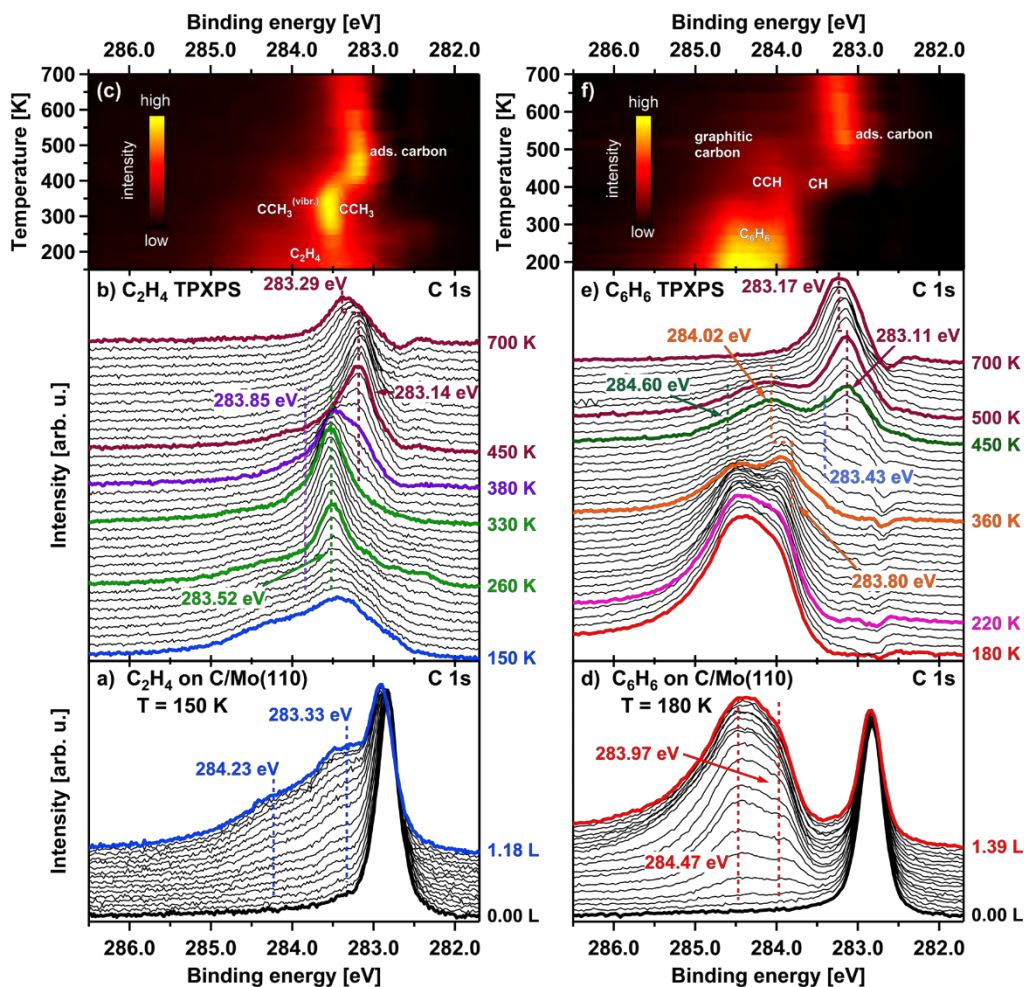


**Figure 5.2:** a) + d)  $C\ 1s$  XPS spectra acquired during low temperature adsorption of  $C_2H_4$  resp.  $C_6H_6$  on monolayer C/Mo(110). b) + e) Corresponding spectra of  $C_2H_4$  resp.  $C_6H_6$  recorded during the temperature-programmed experiment. Note that difference spectra are depicted with the carbide contribution being subtracted. c) + f) Color-coded density plot of the TPXPS experiments shown in b) and e).

coded density plot. At 220 K, a new peak starts to grow at 283.80 eV, which is attributed to an acetylide (CCH) species according to our TPD results (see Figure 5.3a and the discussion below) and results in the literature.<sup>88,101,148-150</sup> This species reaches its maximum coverage at 440 K when chemisorbed benzene has finally vanished. Obviously, benzene reacts not only to CCH, as we detect another species at 283.43 eV, which is assigned to CH. Starting around 380 K, the complete decomposition sets in as indicated by formation of graphitic and adsorbed carbon, see the peaks at 284.60 and 283.11 eV. To support the XPS results, TPD experiments are performed shown in Figure 5.3b. The spectra show two peaks at 357 and 450 K where the first

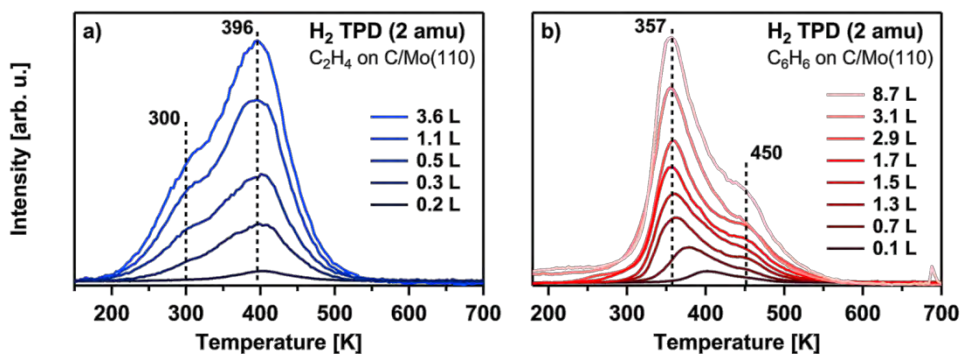


**Figure 5.3:** a) Hydrogen TPD spectra for increasing exposures of a) ethylene and b) benzene on C/Mo(110).

one is located at lower values depending on benzene exposure. The peak at 357 K reflects the desorbing hydrogen that is released during dehydrogenation to the acetylide intermediate. At high exposures, missing space leads to immediate desorption of the hydrogen, whereas at lower exposures a second order desorption is supposed with hydrogen adsorbing on the surface and desorbing associatively. This behavior explains the shift of the first peak to lower temperature with increasing exposure until 1.3 L is reached. For the second peak at 450 K, which is attributed to CCH resp. CH dehydrogenation, no such behavior is observed since the temperature is already above the desorption temperature of H<sub>2</sub>/C/Mo(110) at comparable coverages of H<sub>2</sub>, which leads to immediate desorption. The integration of both TPD peaks delivers a ratio of 1:1 fitting perfectly to the proposed reaction mechanism. Finally, NEXAFS measurements reveal an adsorption geometry with the ring plane being oriented parallel to the surface plane. As a last experiment, we adsorbed the non-aromatic cyclohexane at low temperature and observed a full desorption until 200 K without any reaction of the molecule on the surface.

In conclusion, we compare the reactivity of the two molecules on C/Mo(110) to the Pt(111) surface. The reaction pathway is identical for ethylene but reaction temperatures are lowered by ~85 K. For benzene, the situation is very similar regarding the reaction pathway, but extremely lowered reaction temperatures are found as the acetylide intermediate forms at 220 K, which is about 200 K lower than on Pt(111).



## 6 Summary

Developing alternative energy storage concepts will be a key aspect for the future in order to become independent on fossil fuels. Among the variety of new technologies, the storage of sun energy in strained organic molecules may contribute to this goal. One of the prototype systems in this field is the norbornadiene (NBD)/quadricyclane (QC) system, where the parent NBD compound absorbs and stores solar energy by converting to its strained isomer QC. In a catalytic process, the stored energy can be released on demand. Depending on purpose, this can be performed either heterogeneously for heat output or electrochemically for generating electric power.

To become a viable option, the NBD/QC system needs to be fully optimized. The challenges are shifting the absorption maximum of NBD into the visible region, increasing the energy storage density and half-life of QC, and tailoring efficient catalysts for the cycloreversion from QC to NBD. Moreover, thermal stability ranges and possible decomposition products are of great interest, e.g., when molecular fragments block active catalyst sites or electrode fouling decreases the electric output. Surface science methods provide excellent tools to investigate the basic reaction steps on a catalyst surface and by that its reactivity under ultra clean conditions.

In this context, first UHV experiments on the NBD/QC system have been performed in the framework of this thesis. Starting with NBD/QC on Pt(111), the adsorption and reaction was investigated using UPS, XPS and IRAS in combination with DFT. NBD and QC multilayers were unambiguously identified. In the monolayer region, NBD chemisorbs molecularly at 125 K and preferentially adopts a  $\eta^2:\eta^1$  geometry, as verified by comparison with calculated IR spectra. In this adsorption state, NBD interacts with the Pt surface through one double bond and an agostic interaction involving the bridgehead CH<sub>2</sub> group. The C-H bond involved in the agostic interaction breaks between 190 and 220 K, leading to dehydrogenation and the formation of a norbornadienyl intermediate, which is stable up to approximately 380 K. Contact of QC with the Pt(111) surface triggers immediate cycloreversion to NBD already at 125 K.

The next step was to follow the cycloreversion from QC to NBD on a less reactive surface. For this, the Ni(111) surface has been chosen. Both molecules produce characteristic photoemission spectra in chemisorbed and physisorbed layers at low temperature on Ni(111).

DFT calculations suggest the flat  $\eta^2:\eta^2$  geometry to be the most stable adsorption structure for NBD. For QC, a flat  $\eta^2:\eta^2$  and a side-on  $\eta^2:\eta^1$  geometry are energetically fairly close. For NBD, NEXAFS experiments confirm the adsorption geometry with both double bonds of NBD being oriented parallel to the surface. Upon heating, QC is converted to NBD, which is completed at 168 K. Further heating leads to thermal decomposition of NBD. Starting at 190 K, the formation of benzene ( $C_6H_6$ ) and methylidyne (CH) is observed. This contrasts the situation on Pt(111), where a norbornadienyl species has been identified at similar temperatures. Overall, Ni(111) is found to be less reactive, because on Pt(111) rapid cycloreversion of QC to NBD is observed already at 125 K.

To further optimize the NBD/QC MOST system, 2,3-dibromosubstituted molecules were investigated. The chosen substitution pattern serves as a model system for applicable NBD/QC candidates. The low temperature adsorption of the compounds shows characteristic XP spectra. A detailed analysis of the Br 3d core level reveals partial dissociation of the molecules at  $\sim 110$  K to form chemisorbed Br. TPXPS of  $Br_2$ -NBD shows the decomposition to  $C_6H_6$  and CH at  $\sim 195$  K, accompanied by cleavage of the remaining C-Br bonds.  $Br_2$ -QC converts to  $Br_2$ -NBD starting around 130 K, whereas mostly NBD is formed as the C-Br bond gets cleaved during the conversion. The decomposition to  $C_6H_6$  and CH including the cleavage of the remaining C-Br bonds sets in at  $\sim 195$  K. DFT calculations reveal the most stable adsorption geometries for  $Br_2$ -NBD to be a  $\eta^2:\eta^1$  mode with the Br atoms pointing away from the surface, and for  $Br_2$ -QC a  $\eta^2:\eta^1$  configuration with the Br atoms adsorbed on on-top sites. UP spectra taken during the low temperature adsorption are characteristic for both molecules, whereas during a TPUPS experiment the conversion has not been observed unambiguously. As a result, it can be said that the conversion principally is observed for this system, however, the partial dissociation at low temperature is undesired.

A second direction to optimize heterogeneous reactions is the choice of catalyst material. These materials should exhibit reduced or even avoid precious metal content without losing catalytic activity. One example is the usage of bimetallic surface alloys. In this thesis, a  $Pt_xAg_{1-x}/Pt(111)$  surface was probed using the test molecules CO and ethylene ( $C_2H_4$ ). In a second example, monolayer molybdenum carbide (C/Mo(110)), behaving similarly or even outperforming Pt(111), was probed with  $C_2H_4$ ,  $C_6H_6$  and cyclohexane ( $C_6H_{12}$ ).

For CO adsorbed on  $\text{Pt}_x\text{Ag}_{1-x}/\text{Pt}(111)$  at low temperature, successively on-top and bridge Pt sites are occupied, similar to  $\text{Pt}(111)$ . At saturation, the coverage of the bridge sites is always smaller than that of the on-top sites, and the total coverage depends linearly on the Ag content. As deduced from TPXPS experiments, the desorption temperatures of the CO species on the surface alloys are much higher than on  $\text{Pt}(111)$ . For CO adsorbed on on-top sites, an upward shift of the desorption temperature by 65 K was found for 33% Ag content that increases to  $\sim 105$  K for 68% Ag content. For CO adsorbed on bridge sites, this shift is smaller, with a maximum value of  $\sim 45$  K. The corresponding adsorption energies are thus drastically increased on the surface alloys. For  $\text{C}_2\text{H}_4$ , two different adsorption species were detected, compared to only one on  $\text{Pt}(111)$ . The first one is attributed to  $\text{C}_2\text{H}_4$  adsorbed on Pt islands, whereas the second and lower populated one is assigned to adsorption on Pt atoms in contact with Ag atoms or on mixed Pt-Ag sites. The thermal evolution of  $\text{C}_2\text{H}_4$  resembles the reaction on clean  $\text{Pt}(111)$  concerning intermediate species. As a main product, we identify ethylidyne ( $\text{CCH}_3$ ) due to a unique vibrational splitting in the XP spectra. On the alloys, this intermediate is formed at  $\sim 60$  K lower temperatures than on clean  $\text{Pt}(111)$ . Moreover, full conversion of  $\text{C}_2\text{H}_4$  is observed in contrast to  $\text{Pt}(111)$ , where ethylene partly desorbs as intact molecule. Overall, the observed behavior of CO and  $\text{C}_2\text{H}_4$  indicates that altering the catalyst composition and thus electronic structure can lead to drastic changes in catalytic activity.

Finally, a combined XPS, TPD and NEXAFS investigation was performed on the adsorption and reaction of  $\text{C}_2\text{H}_4$ ,  $\text{C}_6\text{H}_6$  and  $\text{C}_6\text{H}_{12}$  on  $\text{C}/\text{Mo}(110)$ . For  $\text{C}_2\text{H}_4$ , at low temperature two different species grow at a constant relative ratio until saturation of 0.66 ML carbon. We attribute this behavior to two different adsorption sites. NEXAFS indicates that at least one of the two species adsorbs with its molecular axis not parallel to the surface. Upon heating, at 180 K,  $\text{CCH}_3$  forms, which is stable up to 325 K when the decomposition to amorphous carbon sets in, which diffuses into the bulk at elevated temperatures. Corresponding TPD measurements showed hydrogen desorption. The quantification of the spectra agreed well with the observed intermediates. For  $\text{C}_6\text{H}_6$  adsorption, we observed two separate XPS peaks that grow with a constant ratio of 1.0 until saturation of 1.0 ML carbon. We propose that either the carbon atoms in  $\text{C}_6\text{H}_6$  experience two locally different environments with a 1:1 ratio, or that two benzene species are populated.  $\text{C}_6\text{H}_6$  adsorbs parallel to the surface plane as revealed by NEXAFS. Upon heating, we find the formation of a CCH (acetylide) species, which is stable from 230 to 450 K,

while the remaining  $C_6H_6$  is stable on the surface up to 450 K. A second intermediate, forming to a smaller amount, is identified as CH with a stability range from 350 to 410 K. At 380 K, decomposition to amorphous carbon sets in accompanied by a small graphite fraction.  $C_6H_{12}$  only weakly binds to the surface and desorbs without reaction until 200 K. The comparison of the dehydrogenation and decomposition on C/Mo(110) with Pt(111) shows an enhanced reactivity, as indicated by significantly lower onset temperatures for the reaction of  $C_2H_4$  and  $C_6H_6$ . Interestingly, for  $C_6H_{12}$ , the opposite behavior is observed, that is, no decomposition occurs on C/Mo(111), whereas dehydrogenation to  $C_6H_6$  was found on Pt(111).

Overall, this work paves the way for further studies on NBD and QC derivatives under UHV conditions. The reactivity on Pt (111) and Ni (111) was investigated and elucidated in great detail. In addition to the derivatization, suitable and optimized catalysts will have to be looked for in the future. The investigated systems in the second part of this thesis provide a starting point for this. Bimetallic surfaces and molybdenum carbide have proved to be extremely reactive catalysts and could also be used in the conversion of QC to NBD.

## 7 Zusammenfassung

Die Entwicklung alternativer Energiespeicherkonzepte wird ein Kernpunkt in der Zukunft sein um unabhängig von fossilen Brennstoffen zu werden. Unter der Vielzahl neuer Technologien wird die Speicherung von Sonnenenergie in gespannten organischen Molekülen einen Beitrag für dieses Ziel leisten können. Einen Prototyp hierbei stellt das Norbornadien (NBD)/-Quadricyclan (QC)-System dar, bei welchem der Ausgangsstoff NBD Sonnenenergie absorbiert und speichert indem es sich in sein verspanntes Valenzisomer QC umwandelt. In einem katalytischen Prozess kann die gespeicherte Energie nach Bedarf freigesetzt werden. Je nach Verwendungszweck kann dies entweder heterogen für Wärmeabgabe oder elektrochemisch für die Erzeugung von elektrischer Leistung geschehen.

Um als zukünftige Energiequelle zu fungieren, muss das NBD/QC-System vollständig optimiert werden. Die Herausforderungen sind hierbei das Verschieben des Absorptionsmaximums von NBD in den sichtbaren Spektralbereich, die Erhöhung der Energiespeicherdichte und der Halbwertszeit von QC und die Entwicklung effizienter Katalysatoren für die Cycloreversion vom QC zum NBD. Des Weiteren sind thermische Stabilitätsbereiche und mögliche Zersetzungsprodukte von großem Interesse, z.B. wenn Molekülfragmente aktive Katalysatorplätze blockieren oder Elektrodenverschmutzung die Abgabe elektrischer Leistung mindert. Die Methoden der Oberflächenwissenschaft stellen ein ausgezeichnetes Werkzeug dar, um die grundlegenden Reaktionsschritte auf einer Katalysatoroberfläche und damit deren Reaktivität unter hochreinen Bedingungen zu untersuchen.

In diesem Zusammenhang wurden im Rahmen dieser Arbeit UHV-Experimente an dem NBD/QC-System durchgeführt. Zuerst wurde die Adsorption und Reaktion von NBD/QC auf Pt(111) mit UPS, XPS und IRAS kombiniert mit DFT untersucht. Physisorbierte NBD- und QC-Lagen konnten mit UPS und IRAS eindeutig identifiziert werden. In der Monolage chemisorbiert NBD molekular bei 125 K bevorzugt in einer  $\eta^2:\eta^1$  Geometrie was durch Vergleiche mit berechneten IR-Spektren gezeigt werden konnte. Hierbei interagiert NBD mit der Pt-Oberfläche über eine Doppelbindung und eine agostische Wechselwirkung des  $\text{CH}_2$ -Brückenkopfes. Die bei der agostischen Wechselwirkung involvierte C-H-Bindung bricht zwischen 190 und 220 K, was zu einer Dehydrierung und Bildung eines Norbornadienyl-Intermediates führt, welches bis etwa 380 K stabil ist. Der Kontakt von QC mit der Pt(111)-Oberfläche löst bereits bei 125 K eine

sofortige Umwandlung zum NBD aus.

Der nächste Schritt bestand darin, der Cycloreversion von QC zum NBD auf einer weniger reaktiven Oberfläche zu folgen. Dafür wurde die Ni(111)-Oberfläche ausgewählt. Beide Moleküle generieren hierbei charakteristische Photoemissionsspektren in chemisorbierten und physisorbierten Lagen bei tiefer Temperatur. DFT Rechnungen zeigen, dass eine flache  $\eta^2:\eta^2$ -Geometrie die stabilste Adsorptionsstruktur darstellt. Für QC sind die flache  $\eta^2:\eta^2$ - und die seitliche  $\eta^2:\eta^1$ -Geometrie energetisch auf einem ähnlichen Level. Beim NBD bestätigen NEXAFS-Experimente die  $\eta^2:\eta^2$ -Struktur, bei der beide Doppelbindungen parallel zur Oberfläche liegen. Während des Heizens wandelt sich QC zum NBD bis 168 K komplett um. Weiteres Tempern führt zur thermischen Zersetzung von NBD. Beginnend bei 190 K setzt die Bildung von Benzol ( $C_6H_6$ ) and Methyldin (CH) ein. Dies stellt einen Gegensatz zur Situation auf Pt(111) dar, wo eine Norbornadienyl-Spezies bei ähnlicher Temperatur identifiziert wurde. Insgesamt weist Ni(111) eine geringere Reaktivität auf, da auf Pt(111) eine sofortige Umwandlung vom QC zum NBD bereits bei 125 K zu beobachten ist.

In weiteren Experimenten wurden 2,3-dibromosubstituierte Moleküle untersucht. Das gewählte Substitutionsmuster dient als ein Modellsystem für praxistaugliche NBD/QC-Kandidaten. Die Adsorption der Verbindungen bei tiefer Temperatur brachte charakteristische XP-Spektren hervor. Eine detaillierte Analyse des Br 3d Niveaus zeigte eine partielle Dissoziation der Moleküle bei  $\sim 110$  K, was zur Bildung von chemisorbiertem Br führt. TPXPS-Messungen von  $Br_2$ -NBD zeigen die Zersetzung zu  $C_6H_6$  und CH bei  $\sim 195$  K, begleitet von der Spaltung der restlichen C-Br-Bindungen.  $Br_2$ -QC wandelt sich beginnend bei etwa 130 K zu  $Br_2$ -NBD um, wobei sich hauptsächlich NBD bildet, da die C-Br-Bindung während der Umwandlung gespalten wird. Die Zersetzung zu  $C_6H_6$  und CH inklusive der Spaltung der übrigen C-Br-Bindungen beginnt bei  $\sim 195$  K. DFT-Rechnungen identifizieren die stabilsten Adsorptionsgeometrien. Diese sind für  $Br_2$ -NBD eine  $\eta^2:\eta^1$  Struktur, bei der die Br-Atome von der Oberfläche wegzeigen, und für  $Br_2$ -QC eine  $\eta^2:\eta^1$  Konfiguration mit den Br-Atomen auf linear gebundenen Plätzen sitzend. UP-Spektren der Adsorption bei tiefer Temperatur sind für beide Moleküle charakteristisch, wohingegen die Umwandlung mit einem TPUPS-Experiment nicht eindeutig beobachtet werden konnte. Als Fazit kann man sagen, dass die Umwandlung für dieses System grundsätzlich zu beobachten ist, jedoch die partielle Dissoziation bei tiefer Temperatur als unerwünscht zu sehen ist.

Eine zweite Methode zur Optimierung heterogener Reaktionen besteht in der Wahl des Katalysatormaterials. Diese Materialien sollten reduzierten Edelmetallgehalt aufweisen oder gänzlich vermeiden ohne dabei katalytische Aktivität einzubüßen. Ein Beispiel ist die Verwendung von bimetallic Oberflächenlegierungen. In dieser Arbeit wurde eine  $\text{Pt}_x\text{Ag}_{1-x}/\text{Pt}(111)$ -Oberfläche mit CO und Ethylen ( $\text{C}_2\text{H}_4$ ) als Testmolekülen sondiert. In einem zweiten Beispiel wurde einlagiges Molybdän-carbid ( $\text{C}/\text{Mo}(110)$ ), welches sich ähnlich zu  $\text{Pt}(111)$  verhält oder dessen Aktivität sogar übersteigt, mit  $\text{C}_2\text{H}_4$ ,  $\text{C}_6\text{H}_6$  und Cyclohexan ( $\text{C}_6\text{H}_{12}$ ) als Testmolekülen sondiert.

Bei der Adsorption von CO auf  $\text{Pt}_x\text{Ag}_{1-x}/\text{Pt}(111)$  bei tiefer Temperatur werden sukzessive linear gebundene und verbrückte Adsorptionsplätze eingenommen, ähnlich dem Verhalten auf  $\text{Pt}(111)$ . Nach Erreichen der Sättigung ist die Bedeckung von linear gebundenem CO stets größer als jene der verbrückt gebundenen Moleküle, wobei die Gesamtbedeckung linear vom Ag-Gehalt abhängt. Wie mit Hilfe von TPXPS-Experimenten herausgefunden wurde, liegen die Desorptionstemperaturen der beiden CO-Spezies auf den Oberflächenlegierungen wesentlich höher als auf  $\text{Pt}(111)$ . Für linear gebundenes CO wurde ein 65 K großer Verschiebung hin zu höheren Temperaturen bei 33% Ag-Gehalt gefunden, welcher sich auf etwa 105 K für 68% Ag-Gehalt erhöht. Beim verbrückt gebundenen CO ist dieser Verschiebung mit etwa 45 K stets kleiner. Demzufolge sind die zugehörigen Adsorptionsenergien auf den Oberflächenlegierungen auch drastisch erhöht. Bei der Adsorption von  $\text{C}_2\text{H}_4$  wurden zwei Spezies im Vergleich zu nur einer auf  $\text{Pt}(111)$  detektiert. Erstere wird  $\text{C}_2\text{H}_4$ -Adsorption auf Pt-Inseln zugeordnet, wohingegen die andere Spezies der Adsorption auf Pt-Atomen in Kontakt zu Ag-Atomen oder auf gemischten Pt-Ag-Plätzen zugeschrieben werden kann. Die thermische Entwicklung von  $\text{C}_2\text{H}_4$  ähnelt der Reaktion auf  $\text{Pt}(111)$  hinsichtlich der Intermediate. Als Hauptprodukt wird Ethylidin ( $\text{CCH}_3$ ) anhand einer charakteristischen Vibrationsaufspaltung in den XP-Spektren identifiziert. Auf den Legierungen wird dieses Intermediat bei etwa 60 K geringerer Temperatur im Vergleich zu  $\text{Pt}(111)$  gebildet. Zudem findet eine vollständige Umsetzung von  $\text{C}_2\text{H}_4$ , im Gegensatz zu  $\text{Pt}(111)$ , wo  $\text{C}_2\text{H}_4$  teilweise desorbiert, statt. Alles in allem deutet das beobachtete Verhalten von CO und  $\text{C}_2\text{H}_4$  an, dass eine Variation der Katalysatorzusammensetzung und damit der elektronischen Struktur zu einer völlig veränderten katalytischen Aktivität führen kann.

Zuletzt wurde eine kombinierte XPS-, TPD- und NEXAFS-Studie über die Adsorption und Reaktion von  $\text{C}_2\text{H}_4$ ,  $\text{C}_6\text{H}_6$  und  $\text{C}_6\text{H}_{12}$  auf  $\text{C}/\text{Mo}(110)$  durchgeführt. Bei  $\text{C}_2\text{H}_4$  wurden während der

Adsorption bei tiefer Temperatur zwei Spezies, welche mit konstantem relativen Verhältnis bis zur Sättigung von 0.66 ML Kohlenstoff wachsen, gefunden. Dieses Verhalten wird zwei unterschiedlichen Adsorptionsplätzen zugewiesen. Die zugehörigen NEXAFS-Messungen deuten an, dass mindestens eine der beiden Spezies nicht parallel mit seiner Molekülachse zur Oberfläche angeordnet ist. Beim Heizen bildet sich bei 180 K CCH<sub>3</sub>, was bis 325 K stabil ist, während sich amorpher Kohlenstoff formt, der bei erhöhten Temperaturen in das Kristallvolumen diffundiert. Zugehörige TPD-Messungen zeigten die Wasserstoffdesorption, wobei die Quantifizierung der Spektren gut mit den gefundenen Intermediaten übereinstimmte. Für C<sub>6</sub>H<sub>6</sub> wurden zwei getrennte XPS-Peaks beobachtet, welche mit einem konstanten relativen Verhältnis von 1.0 bis zur Sättigung von 1.0 ML Kohlenstoff wachsen. Es wird vermutet, dass sich die Kohlenstoffatome im C<sub>6</sub>H<sub>6</sub> entweder auf zwei lokal verschiedenen Plätzen befinden, die im 1:1 Verhältnis zueinanderstehen, oder dass zwei verschiedene Benzolspezies besetzt werden. C<sub>6</sub>H<sub>6</sub> adsorbiert parallel zur Oberfläche, was aus NEXAFS-Messungen folgt. Während des Heizens bildet sich Acetylid (CCH), welches von 230 bis 450 K stabil ist, wobei das nichtreagierte C<sub>6</sub>H<sub>6</sub> bis 450 K auf der Oberfläche stabil bleibt. Ein weiteres Intermediat, welches nur in geringem Maße entsteht, wurde als CH mit einem Stabilitätsbereich von 350 bis 410 K identifiziert. Mit Erreichen von 380 K setzt die Zersetzung zu amorphem Kohlenstoff ein, was von der Bildung geringer Mengen Carbide begleitet wird. C<sub>6</sub>H<sub>12</sub> bindet nur schwach an die Oberfläche und desorbiert ohne zu reagieren bis 200 K. Der Vergleich des Dehydrierungs- und Zersetzungsverhaltens auf C/Mo(110) mit dem auf Pt(111) offenbart eine erhöhte Reaktivität wie man anhand der niedrigeren Temperaturen, bei denen die Reaktion auf dem Carbide im Fall von C<sub>2</sub>H<sub>4</sub> und C<sub>6</sub>H<sub>6</sub> startet, sieht. Interessanterweise wird für C<sub>6</sub>H<sub>12</sub> ein entgegengesetztes Verhalten beobachtet, nämlich dass keine Zersetzung auf C/Mo(110) stattfindet wohingegen auf Pt(111) eine Dehydrierung zu Benzol gefunden wurde.

Insgesamt konnte mit dieser Arbeit der Grundstein für weitere Studien mit NBD- und QC-Derivaten unter UHV-Bedingungen gelegt werden. Es wurde die Reaktivität auf Pt(111) und Ni(111) detailliert untersucht und aufgeklärt. Neben der Derivatisierung müssen hier in Zukunft geeignete und optimierte Katalysatoren erforscht werden. Einen Ansatzpunkt liefern die untersuchten Systeme im zweiten Teil dieser Arbeit. Bimetallische Oberflächen sowie Molybdän-carbid haben sich als äußerst reaktive Katalysatoren erwiesen und könnten auch bei der Umwandlung von QC zum NBD herangezogen werden.

---

## 8 Literature

1. A. Ali, R. A. Tufa, F. Macedonio, E. Curcio, E. Drioli *Renew. Sust. Energ. Rev.* **2018**, *81*, 1-21.
2. V. Arutyunov, G. Lisichkin *Russ. Chem. Rev.* **2017**, *86*, 777-804.
3. D. Teichmann, W. Arlt, P. Wasserscheid, R. Freymann *Energy Environ. Sci.* **2011**, *4*, 2767-2773.
4. British Petroleum *BP Statistical Review of World Energy 2017*, Report 66, London, 2017.
5. H. Ibrahim, A. Ilinca, J. Perron *Renew. Sust. Energ. Rev.* **2008**, *12*, 1221-1250.
6. J. Baker *Energy Policy* **2008**, *36*, 4368-4373.
7. B. Dunn, H. Kamath, J.-M. Tarascon *Science* **2011**, *334*, 928-935.
8. Z. Yang, J. Zhang, M. Kintner-Meyer, X. Lu, D. Choi, J. Lemmon, J. Liu *Chem. Rev.* **2011**, *111*, 3577-3613.
9. A. Fujishima, K. Honda *Nature* **1972**, *238*, 37-38.
10. N. Lewis, D. Nocera *PNAS* **2006**, *103*, 15729-15735.
11. H. Gray *Nat. Chem.* **2009**, *1*, 1-7.
12. A. Yilanci, I. Dincer, H. Ozturk *Prog. Energy Combust. Sci.* **2009**, *35*, 231-244.
13. A. Magnuson, M. Anderlund, O. Johansson, P. Lindblad, R. Lomoth, T. Polivka, S. Ott, K. Stensjö, S. Styring, V. Sundström et al. *Acc. Chem. Res.* **2009**, *42*, 1899-1909.
14. P. Tran, L. Wong, J. Barber, J. Loo *Energy Environ. Sci.* **2012**, *5*, 5902-5918.
15. S. Dahl, I. Chorkendorff *Nat. Mater.* **2012**, *11*, 100-101.
16. K. Joya, Y. Joya, K. Ocakoglu, R. van de Krol *Angew. Chem. Int. Ed.* **2013**, *52*, 10426-10437.
17. F. Chowdhury, M. Trudeau, H. Guo, Z. Mi *Nat. Commun.* **2018**, *9*, 1707 1-9.
18. J. Yu, J. Low, W. Xiao, P. Zhou, M. Jaroniec *J. Am. Chem. Soc.* **2014**, *136*, 8839-8842.
19. E. Maginn *J. Phys. Chem. Lett.* **2010**, *1*, 3478-3479.
20. L. Yuan, Y.-J. Xu *Appl. Surf. Sci.* **2015**, *342*, 154-167.

21. S. N. Habisreutinger, L. Schmidt-Mende, J. K. Stolarczyk *Angew. Chem. Int. Ed.* **2013**, *52*, 7372-7408.
22. J. Low, J. Yu, W. Ho *J. Phys. Chem. Lett.* **2015**, *6*, 4244-4251.
23. D. Teichmann, K. Stark, K. Müller, G. Zöttl, P. Wasserscheid, W. Arlt *Energy Environ. Sci.* **2012**, *5*, 9044-9054.
24. D. Teichmann, W. Arlt, P. Wasserscheid *Int. J. Hydrog. Energy* **2012**, *37*, 18118-18132.
25. C. Gleichweit, M. Amende, S. Schernich, W. Zhao, M. P. A. Lorenz, O. Höfert, N. Brückner, P. Wasserscheid, J. Libuda, H.-P. Steinrück et al. *Chem. Sus. Chem.* **2013**, *6*, 974-977.
26. M. Amende, C. Gleichweit, K. Werner, S. Schernich, W. Zhao, M. P. A. Lorenz, O. Höfert, C. Papp, M. Koch, P. Wasserscheid et al. *ACS Catal.* **2014**, *4*, 657-665.
27. T. He, Q. Pei, P. Chen *J. Energy Chem.* **2015**, *24*, 587-594.
28. E. Durgun, J. C. Grossman *J. Phys. Chem. Lett.* **2013**, *4*, 854-860.
29. A. M. Kolpak, J. C. Grossman *Nano Lett.* **2011**, *11*, 3156-3162.
30. T. J. Kucharski, N. Ferralis, A. M. Kolpak, J. O. Zheng, D. G. Nocera, J. C. Grossman *Nat. Chem.* **2014**, *6*, 441-447.
31. H. M. D. Bandara, S. C. Burdette *Chem. Soc. Rev.* **2012**, *41*, 1809-1825.
32. C. Slavov, C. Yang, L. Schweighauser, C. Boumrifak, A. Dreuw, H. A. Wegner, J. Wachtveitl *Phys. Chem. Chem. Phys.* **2016**, *18*, 14795-14804.
33. K. Masutani, M. Morikawa, N. Kimizuka *Chem. Commun.* **2014**, *50*, 15803-15806.
34. A. Lennartson, A. Roffey, K. Moth-Poulsen *Tetrahedron Letters* **2015**, *56*, 1457-1465.
35. C. Bastianelli, V. Caia, G. Cum, R. Gallo, V. Mancini *J. Chem. Soc. Perkin trans.* **1991**, *2*, 679-683.
36. G. Jones, T. E. Reinhardt, W. R. Bergmark *Solar Energy* **1978**, *20*, 241-248.
37. B. D. Sherman, M. D. Vaughn, J. J. Bergkamp, D. Gust, A. L. Moore, T. A. Moore *Photosynth. Res.* **2014**, *120*, 59-70.
38. K. Moth-Poulsen, D. Coso, K. Börjesson, N. Vinokurov, S. Meier, A. Majumdar, K. Vollhardt, R. Segalman *Energy Environ. Sci.* **2012**, *5*, 8534-8537.
39. K. P. C. Vollhardt, T. W. Weidman *J. Am. Chem. Soc.* **1983**, *105*, 1677-1679.

- 
40. R. Boese, J. K. Cammack, A. J. Matzger, K. Plug, W. B. Tolman, K. P. C. Vollhardt, T. W. Weidman *J. Am. Chem. Soc.* **1997**, *119*, 6757-6773.
  41. M. R. Harpham, S. C. Nguyen, Z. Hou, J. C. Grossman, C. B. Harris, M. W. Mara, A. B. Stickrath, Y. Kanai, A. M. Kolpak, D. Lee et al. *Angew. Chem. Int. Ed.* **2012**, *51*, 7692-7696.
  42. A. Lennartson, A. Lundin, K. Börjesson, V. Gray, K. Moth-Poulsen *Dalton Trans.* **2016**, *45*, 8740-8744.
  43. Y. Kanai, V. Srinivasan, S. K. Meier, K. P. C. Vollhardt, J. C. Grossman *Angew. Chem. Int. Ed.* **2010**, *49*, 8926-8929.
  44. G. Hammond, P. Wyatt, C. D. Boer, N. Turro *J. Am. Chem. Soc.* **1964**, *86*, 2532-2533.
  45. C. Smith *Org. Syn.* **1971**, *51*, 133-133.
  46. D. Schwendiman, C. Kutal *J. Am. Chem. Soc.* **1977**, *99*, 5677-5682.
  47. K. Maruyama, K. Terada, Y. Yamamoto *J. Org. Chem.* **1981**, *46*, 5294-5300.
  48. D. J. Fife, K. W. Morse, W. M. Moore *J. Am. Chem. Soc.* **1983**, *105*, 7404-7407.
  49. K. Maruyama, H. Tamiaki, S. Kawabata *J. Org. Chem.* **1985**, *50*, 4742-4749.
  50. Z.-I. Yoshida *J. Photochem.* **1985**, *29*, 27-40.
  51. Y. Harel, A. Adamson, C. Kutal, P. Grutsch, K. Yasufuku *J. Phys. Chem.* **1987**, *91*, 901-904.
  52. V. Bren', A. Dubonosov, V. Minkin, V. Chernoiivanov *Russ. Chem. Rev.* **1991**, *60*, 451-469.
  53. A. Cuppoletti, J. Dinnocenzo, J. Goodman, I. Gould *J. Phys. Chem. A* **1999**, *103*, 11253-11256.
  54. A. Dubonosov, V. Bren, V. Chemoivanov *Russ. Chem. Rev.* **2002**, *71*, 917-927.
  55. A. Dias, M. M. d. Piedade, J. M. Simoes, J. Simoni, C. Teixeira, H. Diogo, Y. Meng-Yan, G. Pilcher *J. Chem. Thermodynamics* **1992**, *24*, 439-447.
  56. M. Fischer, M. Werber, P. Schwartz *Energy Policy* **2009**, *37*, 2639-2641.
  57. S. Miki, Y. Asako, Z. Yoshida *Chem. Lett.* **1987**, *16*, 195-198.
  58. M.-C. Tsai, J. Stein, C. Friend, E. Muettertides *J. Am. Chem. Soc.* **1982**, *104*, 3533-3534.
  59. M. Hostetler, R. Nuzzo, G. Girolami, L. Dubois *Organometallics* **1995**, *14*, 3377-3384.
-

60. O. Brummel, D. Besold, T. Döpfer, Y. Wu, S. Bochmann, F. Lazzari, F. Waidhas, U. Bauer, P. Bachmann, C. Papp et al. *ChemSusChem* **2016**, *9*, 1424-1432.
61. M. Quant, A. Lennartson, A. Dreos, M. Kuisma, P. Erhart, K. Börjesson, K. Moth-Poulsen *Chem. Eur. J.* **2016**, *22*, 13265-13274.
62. K. Jorner, A. Dreos, R. Emanuelsson, O. E. Bakouri, I. Galván, K. Börjesson, F. Feixas, R. Lindh, B. Zietz, K. Moth-Poulsen et al. *J. Mater. Chem A* **2017**, *5*, 12369-12378.
63. A. Dreos, K. Börjesson, Z. Wang, A. Roffey, Z. Norwood, D. Kushnir, K. Moth-Poulsen *Energy Environ. Sci.* **2017**, *10*, 728-734.
64. A. Dreos, Z. Wang, J. Udmark, A. Ström, P. Erhart, K. Börjesson, M. Nielsen, K. Moth-Poulsen *Adv. Energy Mater.* **2018**, 1703401 1-9.
65. M. Manso, A. Petersen, Z. Wang, P. Erhart, M. Nielsen, K. Moth-Poulsen *Nat. Commun.* **2018**, DOI: 10.1038/s41467-018-04230-8.
66. J. Schiff *Briefwechsel zwischen Goethe und Johann Wolfgang Döbereiner, 1810-1830*, Verlag Böhlau, 1914.
67. P. Sabatier *Ber. Dtsch. Chem. Ges.* **1911**, *44*, 1984-2001.
68. G. Ertl, H. Knözinger, F. Schüth, J. Weitkamp *Handbook of Heterogeneous Catalysis*, 2nd ed., Wiley-VCH, Weinheim, 2008.
69. J. Trillo, G. Munuera, J. Criado *Cat. Rev.* **1972**, *7*, 51-86.
70. J. Sinfelt *Bimetallic Catalysts: Discoveries, Concepts and Applications*, Wiley, New York, 1983.
71. D. Woodruff *The Chemical Physics of Solid Surfaces, Vol. 10 Surface Alloys and Alloy Surfaces*, Elsevier, Amsterdam, 2002.
72. C. Campbell *Annu. Rev. Phys. Chem.* **1990**, *41*, 775-837.
73. V. Ponec *Appl. Catal. A* **2001**, *222*, 31-45.
74. J. Clarke *Chem. Rev.* **1975**, *75*, 291-305.
75. J. Rodriguez *Surf. Sci. Rep.* **1996**, *24*, 223-287.
76. V. Stamenkovic, B. Mun, M. Arenz, K. Mayrhofer, C. Lucas, G. Wang, P. Ross, N. Markovic *Nat. Mater.* **2007**, *6*, 241-247.
77. V. Ponec, W. Sachtler *J. Catal.* **1972**, *24*, 250-261.
78. B. Hammer, J. Nørskov *Adv. Catal.* **2000**, *45*, 71-129.

- 
79. A. L. Walter, F. Schiller, M. Corso, L. R. Merte, F. Bertram, J. Lobo-Checa, M. Shipilin, J. Gustafson, E. Lundgren, A. N. Brion-Rios et al. *Nat. Commun.* **2015**, *6*, 8903-8910.
  80. R. B. Levy, M. Boudart *Science* **1973**, *181*, 547-549.
  81. S. Oyama *Catal. Today* **1992**, *15*, 179-200.
  82. J. Chen *Chem. Rev.* **1996**, *96*, 1477-1498.
  83. H. Hwu, J. Chen *Chem. Rev.* **2005**, *105*, 185-212.
  84. W. Chen, J. Muckerman, E. Fujita *Chem. Comm.* **2013**, *49*, 8896-8909.
  85. B. Frühberger, J. G. Chen *Surf. Sci.* **1995**, *342*, 38-46.
  86. B. Frühberger, J. G. Chen *J. Am. Chem. Soc.* **1996**, *118*, 11599-11609.
  87. B. Frühberger, J. G. Chen, J. Eng, B. E. Bent *J. Vac. Sci. Technol. A* **1996**, *14*, 1475-1481.
  88. J. Eng, B. E. Bent, B. Frühberger, J. G. Chen *J. Phys. Chem. B* **1997**, *101*, 4044-4054.
  89. C. Gleichweit, C. Neiss, S. Maisel, U. Bauer, F. Späth, O. Höfert, F. Vollnhals, M. Drost, H. Marbach, A. Görling et al. *Phys. Rev. B* **2015**, *92*, 014114.
  90. C. Gleichweit, C. Neiss, S. Maisel, U. Bauer, F. Späth, O. Höfert, A. Görling, H.-P. Steinrück, C. Papp *J. Phys. Chem. C* **2017**, *121*, 3133-3142.
  91. J. G. Chen, B. Frühberger *Surf. Sci.* **1996**, *367*, L102-L110.
  92. J. A. Rodriguez, F. Illas *Phys. Chem. Chem. Phys.* **2012**, *14*, 427-438.
  93. J. Falta, T. Möller *Forschung mit Synchrotronstrahlung*, Vieweg+Teubner, Wiesbaden, 2010.
  94. J. Jackson *Classical Electrodynamics*, Wiley, New York, 1975.
  95. Helmholtz-Zentrum Berlin, [https://www.helmholtz-berlin.de/media/media/zentrum/grossgeraete/bessy/ring01\\_1.jpg](https://www.helmholtz-berlin.de/media/media/zentrum/grossgeraete/bessy/ring01_1.jpg) (accessed 17.06.2018).
  96. H. Hertz *Ann. Physik* **1887**, *267*, 983-1000.
  97. A. Einstein *Ann. Physik* **1905**, *322*, 132-148.
  98. D. Briggs, M. Seah *Practical Surface Analysis Volume 1 - Auger and X-ray Photoelectron Spectroscopy*, John Wiley & Sons Ltd, Chichester, 1990.
  99. S. Suga, A. Sekiyama *Photoelectron Spectroscopy Bulk and Surface Electronic Structures*, Springer-Verlag, Berlin Heidelberg, 2014.
-

100. S. Hüfner *Photoelectron Spectroscopy: Principles and Applications*, Springer, Berlin Heidelberg New York, 2003.
101. C. Papp, H.-P. Steinrück *Surf. Sci. Rep.* **2013**, *68*, 446-484.
102. J. Muijsers, J. Niemantsverdriet, I. Wehman-Ooyevaar, D. Grove, G. v. Koten *Inorg. Chem.* **1991**, *31*, 2655-2658.
103. H.-P. Steinrück *Vacuum* **1994**, *45*, 715-731.
104. H.-P. Steinrück *J. Phys.: Condens. Matter* **1996**, *8*, 6465-6509.
105. A. Liebsch *Physical Review Letters* **1974**, *32*, 1203-1206.
106. D. Woodruff *Surf. Sci.* **1994**, *299*, 183-198.
107. M. Seah, W. Dench *Surf. Interface Anal.* **1979**, *1*, 2-11.
108. I. Niedermaier, C. Kolbeck, H.-P. Steinrück, F. Maier *Rev. Sci. Instrum.* **2016**, *87*, 045105 1-14.
109. S. Doniach, M. Šunjić *J. Phys. C: Solid State Phys.* **1970**, *3*, 285-291.
110. M. Kinne. Kinetische Untersuchungen von Oberflächenreaktionen mittels hochaufgelöster Röntgen-Photoelektronenspektroskopie - Oxidation von CO auf Pt(111) und zugehörige Elementarschritte. Ph. D. thesis, Friedrich-Alexander-Universität Erlangen-Nürnberg, Erlangen, 2004.
111. J. Stöhr *NEXAFS Spectroscopy*, Springer-Verlag, Berlin Heidelberg New York, 2003.
112. J. Niemantsverdriet *Spectroscopy in Catalysis*, Wiley-VCH, Weinheim, 2007.
113. D. King *Surf. Sci.* **1975**, *47*, 384-402.
114. R. Masel *Principles of Adsorption and Reaction on Solid Surfaces*, Wiley, New York, 1996.
115. E. Habenschaden, J. Küppers *Surf. Sci.* **1984**, *138*, L147-L150.
116. P. Redhead *Vacuum* **1962**, *12*, 203-211.
117. A. Baraldi, G. Comelli, S. Lizzit, D. Cocco, G. Paolucci, R. Rosei *Surf. Sci.* **1996**, *367*, L67-L72.
118. C. Gleichweit. Dehydrogenation of Liquid Organic Hydrogen Carriers on Model Catalyst Surfaces. Ph. D. thesis, Friedrich-Alexander-Universität Erlangen-Nürnberg, Erlangen, 2015.
119. G. Held, S. Uremovic, C. Stellwag, D. Menzel *Rev. Sci. Instrum.* **1996**, *67*, 378-383.

- 
120. W. Braun. Adsorption und Koadsorption kleiner Moleküle auf Übergangsmetallen und ultradünnen Übergangsmetallschichten. Ph. D. thesis, Friedrich-Alexander-Universität Erlangen-Nürnberg, Erlangen, 2003.
121. P. Feulner, D. Menzel *J. Vac. Sci. Technol.* **1980**, *17*, 662-663.
122. M. Kinne, T. Fuhrmann, C. Whelan, J. Zhu, J. Pantförder, M. Probst, G. Held, R. Denecke, H.-P. Steinrück *J. Chem. Phys.* **2002**, *117*, 10852-10859.
123. J. S. McEwen, S. H. Payne, H. J. Kreuzer, M. Kinne, R. Denecke, H.-P. Steinrück *Surf. Sci.* **2003**, *545*, 47-69.
124. C. Papp, T. Fuhrmann, B. Tränkenschuh, R. Denecke, H.-P. Steinrück *Phys. Rev. B* **2006**, *73*, 235426 1-9.
125. C. Papp, R. Denecke, H.-P. Steinrück *Langmuir* **2007**, *23*, 5541-5547.
126. C. Gleichweit, M. Amende, O. Höfert, T. Xu, F. Späth, N. Brückner, P. Wasserscheid, J. Libuda, H.-P. Steinrück, C. Papp *J. Phys. Chem. C* **2015**, *119*, 20299-20311.
127. A. Hensley, C. Wöckel, C. Gleichweit, K. Gotterbarm, C. Papp, H.-P. Steinrück, R. Denecke, J.-S. McEwen *J. Phys. Chem. C* **2018**, *122*, 4261-4273.
128. M. Laurin *J. Chem. Educ.* **2013**, *90*, 944-946.
129. M. Hostetler, R. Nuzzo, G. Girolami *J. Am. Chem. Soc.* **1995**, *117*, 1814-1827.
130. M. Hoffmann *Surf. Sci. Rep.* **1983**, *3*, 107-192.
131. M. Schmid, W. Hieringer, C. Schmitz, H.-P. Steinrück, M. Sokolowski, M. Gottfried *J. Phys. Chem. C* **2011**, *115*, 14869-14875.
132. X.-L. Zhou, F. Solymosi, P. Blass, K. Cannon, J. White *Surf. Sci.* **1989**, *219*, 294-316.
133. M. Chen, J. Xiao, H.-P. Steinrück, S. Wang, W. Wang, N. Lin, W. Hieringer, M. Gottfried *J. Phys. Chem. C* **2014**, *118*, 6820-6830.
134. E. Marsh, F. Tabares, M. Schneider, T. Gilton, W. Meier, J. Cowin *J. Chem. Phys.* **1989**, *92*, 2004-2014.
135. J. Tsay, C. Shern *CJP* **1996**, *34*, 130-137.
136. H. Röder, R. Schuster, H. Brune, K. Kern *Phys. Rev. Lett.* **1993**, *71*, 2086-2089.
137. U. Strüber, J. Küppers *Surf. Sci. Lett.* **1993**, *294*, L924-L928.
138. J. Tsay, Y. Yao, C. Shern *Phys. Rev. B* **1998**, *58*, 3609-3612.
139. T. Diemant, K. Schüttler, R. Behm *ChemPhysChem* **2015**, *16*, 2943-2952.
-

140. K. Schüttler, L. Mancera, T. Diemant, A. Groß, R. Behm *Surf. Scie.* **2016**, *650*, 237-254.
141. W. Hansen, M. Bertolo, K. Jacobi *Surf. Sci.* **1991**, *253*, 1-12.
142. T. Fuhrmann, M. Kinne, B. Tränkenschuh, C. Papp, J. F. Zhu, R. Denecke, H.-P. Steinrück *New J. Phys.* **2005**, *7*, 107 1-19.
143. H.-P. Steinrück, T. Fuhrmann, C. Papp, B. Tränkenschuh, R. Denecke *J. Chem. Phys.* **2006**, *125*, 204706 1-8.
144. C. Gleichweit, M. Amende, U. Bauer, S. Schernich, O. Höfert, M. P. A. Lorenz, W. Zhao, M. Müller, M. Koch, P. Bachmann et al. *J. Chem. Phys.* **2014**, *140*, 204711 1-9.
145. M. P. A. Lorenz, T. Fuhrmann, R. Streber, A. Bayer, F. Bebensee, K. Gotterbarm, M. Kinne, B. Tränkenschuh, J. F. Zhu, C. Papp et al. *J. Chem. Phys.* **2010**, *133*, 014706 1-6.
146. K. Griffiths, W. N. Lennard, I. V. Mitchell, P. R. Norton *Surf. Sci. Lett.* **1993**, *284*, L389-L393.
147. M. Hills, J. Parmeter, C. Mullins, W. Weinberg *J. Am. Chem. Soc.* **1986**, *108*, 3554-3562.
148. B. E. Koel, J. E. Crowell, B. E. Bent, C. M. Mate, G. A. Somorjai *J. Phys. Chem.* **1986**, *90*, 2949-2956.
149. R. Neubauer, C. M. Whelan, R. Denecke, H.-P. Steinrück *J. Chem. Phys.* **2003**, *119*, 1710-1718.
150. O. Höfert, M. P. A. Lorenz, R. Streber, W. Zhao, A. Bayer, H.-P. Steinrück, C. Papp *J. Chem. Phys.* **2013**, *139*, 164706 1-7.

## 9 Danksagung

Mein besonderer Dank gilt Herrn Prof. Dr. Hans-Peter Steinrück unter dessen ausgezeichneter Betreuung eine nahezu perfekte Arbeitsatmosphäre möglich war. Einerseits waren motivierende, konstruktive und progressive Diskussionen sachlicher Natur jederzeit möglich, zum anderen war eine freundliche und faire Behandlung im nichtakademischen und menschlichen Bereich stets gegeben. Zudem wird das Arbeiten durch zahlreiche soziale Aktivitäten am Lehrstuhl von Prof. Steinrück ungemein erleichtert.

Des Weiteren möchte ich mich ausdrücklich bei Herrn PD Dr. Christian Papp als unmittelbarem Vorgesetzten und Leiter der Synchrotron-Arbeitsgruppe bedanken. Als erster Ansprechpartner bei wissenschaftlichen und auch organisatorischen Anliegen war er immer erreichbar und eine unverzichtbare Hilfe.

Ein Großteil der Daten dieser Arbeit wurde in Berlin am Synchrotron erzeugt, wobei für die Messungen selbst und den Auf- und Abbau der Anlage Teamwork gefragt ist. Für die tatkräftige Unterstützung dabei danke ich meinen Kollegen Herrn Florian Späth, Herrn Philipp Bachmann, Herrn Fabian Düll und Herrn Johann Steinhauer und ehemaligen Kollegen Herrn Dr. Oliver Höfert, Herrn Dr. Christoph Gleichweit, Frau Dr. Karin Gotterbarm und Herrn Dr. Wei Zhao.

Im Rahmen der guten Kooperation mit der Theoretischen Chemie, die Dichtefunktionaltheorie-Rechnungen beigetragen hat, möchte ich mich bei Herrn Lukas Fromm, Herrn Tibor Döpfer und Herrn PD Dr. Wolfgang Hieringer aus der Arbeitsgruppe von Herrn Prof. Dr. Andreas Görling bedanken. Genauso entscheidend war die Versorgung mit selbst synthetisierten Substanzen und Derivaten aus der Organischen Chemie, wofür ich Herrn Cornelius Weiß und Frau Ute Pinkert aus der Arbeitsgruppe von Herrn Prof. Dr. Andreas Hirsch meinen Dank aussprechen will. In diesem Zug ist auch Frau Susanne Mohr aus der Arbeitsgruppe von Herrn Prof. Dr. Jörg Libuda zu nennen, die mit Infrarotmessungen erheblich zu einer Publikation beigetragen hat.

Während der Promotionsphase wurde eine Masterarbeit von Herrn Philipp Bachmann und drei Bachelorarbeiten von Herrn Joshua Lorona Ornelas, Frau Kristina Schall und Frau Jasmin Eisenkolb unter meiner Anleitung angefertigt. Die gewonnenen Ergebnisse wurden zum

Teil in den Publikationen verwendet und in diesem Zusammenhang möchte ich mich für die gute Zusammenarbeit bedanken.

Um das Funktionieren der Anlage und aller zugehörigen Komponenten zu gewährleisten war der technische Support von Herrn Bernd Kreß (Vakuum-Ingenieur) und Herrn Hans-Peter Bäumler (Elektroniker) essentiell. Hierbei ist vor allem die ständige Wartung und Verbesserung des NEXAFS Systems zu nennen. Außerdem bedanke ich mich bei Herrn Friedhold Wölfel als Leiter der Mechanikerwerkstatt und seinem kompletten Team für das zuverlässige Ausführen von Reparaturarbeiten und die Hilfe bei der technischen Umsetzung von neuen UHV-Komponenten.

Schließlich danke ich meinen Eltern Robert und Eleonore, meiner Schwester Sandra und meiner Freundin Katharina, die mir immer eine Stütze waren und die nötige Geduld, auch in schwierigen Lagen, aufgebracht haben.

## 10 Curriculum vitae

### Udo Bauer

---

<b>Date of Birth</b>	11.07.1987
<b>Place of Birth</b>	Gunzenhausen, Germany
<b>Academic Degree</b>	Master of Science (M. Sc.)

### School & Academic Education

---

<b>since 01/2014</b>	<b>Ph.D. Study</b> (Dr. rer. Nat.) Friedrich-Alexander-University Erlangen-Nürnberg Erlangen, Germany
<b>10/2011 – 11/2013</b>	<b>Master of Science in Chemistry</b> (M. Sc.) Title of Master Thesis: <i>“In-situ HR-XPS Investigation of the Dehydrogenation of N-alkyl-carbazoles on Pt(111) and the Preparation of Mo<sub>2</sub>C/Mo(100) a New Noble Metal Free Dehydrogenation Catalyst”</i> Friedrich-Alexander-Universität Erlangen-Nürnberg Erlangen, Germany
<b>10/2008 – 10/2011</b>	<b>Bachelor of Science in Chemistry</b> (B. Sc.) Title of Bachelor Thesis: <i>“Herstellung von N-dotiertem Graphen auf Ni(111) durch Beschuss mit niederenergetischen N<sub>2</sub><sup>+</sup>-Ionen”</i> Friedrich-Alexander-Universität Erlangen-Nürnberg Erlangen, Germany
<b>09/1998 – 06/2007</b>	<b>Allgemeine Hochschulreife</b> Simon-Marius-Gymnasium Gunzenhausen, Germany
<b>09/1994 – 07/1998</b>	<b>Elementary School</b> Volksschule Altmühlsee Pflaumfeld/Stetten, Germany

### Work Experience

---

<b>04/2008 – 08/2008</b>	<b>Order Picker</b> Henkel AG & Co. KGaA Wassertrüdingen, Germany
<b>07/2007 – 03/2008</b>	<b>Military Duty</b> 3./Panzergrenadierbataillon 112 Regen, Germany

---



---

## A Appendix [P1-P5]

- [P1] *Catalytically Triggered Energy Release from Strained Organic Molecules: The Surface Chemistry of Quadricyclane and Norbornadiene on Pt(111)*  
**U. Bauer**, S. Mohr, T. Döpfer, P. Bachmann, F. Späth, F. Düll, M. Schwarz, O. Brummel, L. Fromm, U. Pinkert, A. Görling, A. Hirsch, J. Bachmann, H.-P. Steinrück, J. Libuda, C. Papp  
*Chem. Eur. J.* **2017**, *23*, 1613-1622, DOI: [10.1002/chem.201604443](https://doi.org/10.1002/chem.201604443).
- [P2] *Controlled Catalytic Energy Release of the Norbornadiene/Quadricyclane Molecular Solar Thermal Energy Storage System on Ni(111)*  
**U. Bauer**, L. Fromm, C. Weiß, P. Bachmann, F. Späth, F. Düll, J. Steinhauer, W. Hieringer, A. Görling, A. Hirsch, H.-P. Steinrück, C. Papp  
*J. Phys. Chem. C* **2018**, *accepted*, DOI: [10.1021/acs.jpcc.8b03746](https://doi.org/10.1021/acs.jpcc.8b03746).
- [P3] *Surface Chemistry of 2,3-Dibromosubstituted Norbornadiene/Quadricyclane as Molecular Solar Thermal Energy Storage System on Ni(111)*  
**U. Bauer**, L. Fromm, S. Matysik, C. Weiß, F. Späth, P. Bachmann, F. Düll, J. Steinhauer, A. Görling, A. Hirsch, H.-P. Steinrück, C. Papp  
*In preparation and to be submitted.*
- [P4] *Reactivity of CO and C<sub>2</sub>H<sub>4</sub> on Bimetallic Pt<sub>x</sub>Ag<sub>1-x</sub>/Pt(111) Surface Alloys Investigated by High-Resolution X-ray Photoelectron Spectroscopy*  
**U. Bauer**, F. Späth, F. Düll, P. Bachmann, J. Steinhauer, H.-P. Steinrück, C. Papp  
*ChemPhysChem* **2018**, *19*, 1432-1440, DOI: [10.1002/cphc.201800044](https://doi.org/10.1002/cphc.201800044).
- [P5] *Reactivity Studies of Ethylene, Benzene and Cyclohexane on Carbide-Modified Mo(110) Using High Resolution X-ray Photoelectron Spectroscopy*  
**U. Bauer**, C. Gleichweit, O. Höfert, F. Späth, K. Gotterbarm, H.-P. Steinrück, C. Papp  
*Surf. Sci.* **2018**, *accepted*, DOI: [10.1016/j.susc.2018.01.001](https://doi.org/10.1016/j.susc.2018.01.001).



## B Appendix

### UHV UV LED

During the period of this thesis a self-built UHV UV-LED, shown in Figure B1, was tested under measurement conditions in the synchrotron machine (see Chapter 3.1). The mounted UV LED of type ‘CUN6AF4A’ was bought from Neumüller Elektronik GmbH ([www.neumüller.com](http://www.neumüller.com)). In the following, a brief overview of the most important technical data is presented, a full description can be viewed in the technical data sheet<sup>1</sup>:

L / W / H	6.3 mm / 6.3 mm / 1.4 mm
Wavelength	365 nm
Line width	9 nm
Radiation power	2350 mW
Forward current	1000 mA
Forward voltage	7.8 V
Operation temperature	-10 – 85 °C
Emission angle	116°

In Figure B1, one can see the setup of the UHV LED. It consists of a CF 40 flange where two Cu rods and a support rod are mounted. Between the two Cu rods, a voltage is applied, typically 7.8 V, which may be lower when performed with a tunable transformer leading to a lower radiation power of the LED. The support rod serves for stabilization of the construct due to the relatively large length/mass ratio of the Cu rods. Furthermore, to increase stability several ceramics are mounted in between the Cu rods. At the end of the Cu rods, two rectangular Cu plates are soldered for better cooling capacity during operation of the LED. Finally, the LED is soldered on top of the two Cu plates. At one of the Cu plates, ideally near to the LED, a thermocouple is spot-welded for temperature measurement. As can be seen from the technical data, temperature control is important during operation, as the LED may undergo irreversible damage when temperatures are too high. Experience has shown that temperatures up to ~110-120 °C for maximum 1 minute are possible without damaging the LED. In order to put the LED in front of the sample in the analyzer chamber, a suitable Z-shift is included.

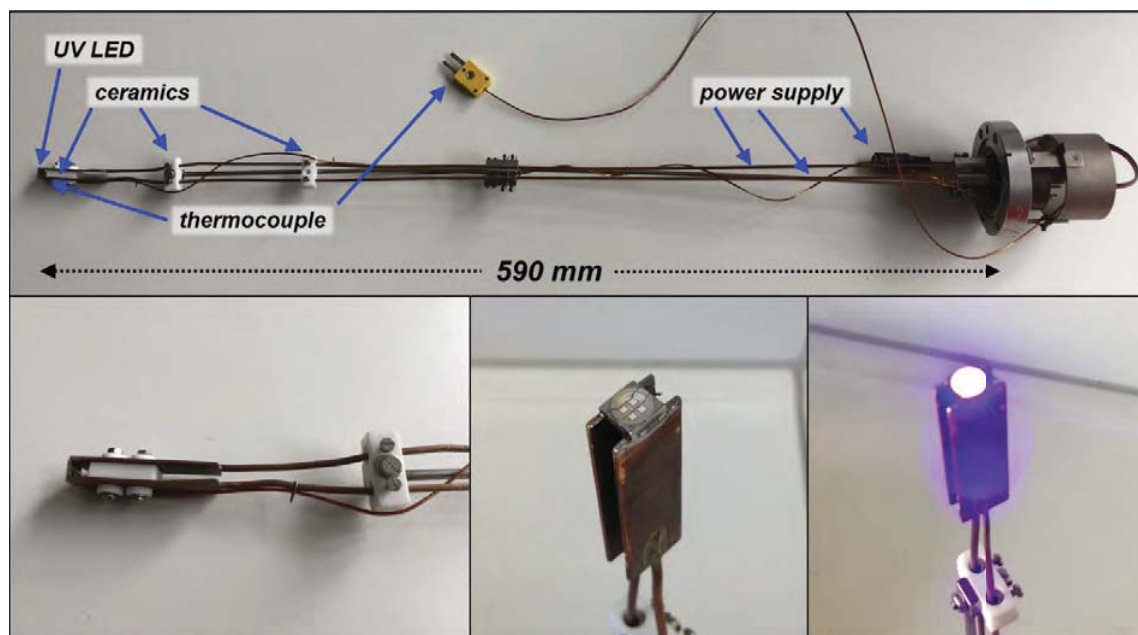


**Figure B1:** Pictures of the self-built UHV UV LED.

Principally, the LED works under UHV conditions. However, the problem during first experiments was a drastic degassing of the LED, even after several cycles of degassing before. The base pressure in the separated LED part was in the  $10^{-10}$  Torr regime after bakeout. However, when the hand valve to the analyzer chamber was opened and the LED operated, the pressure was rising to  $\sim 10^{-7}$ - $10^{-8}$  Torr. This problem could not be fixed so far, and thus, the first experiments were unusable due to high pollution of residual gases and dirt on the sample. A solution to this issue could be, to enhance the cooling by, e.g., larger Cu blocks instead of plates or to incorporate a liquid nitrogen cooling system. By doing so, longer degassing cycles can be performed, probably leading to much less pollution on the sample during operation, and thus, evaluable spectra/experiments.

## UV irradiation apparatus

As prices for synthesized QC from companies are in the magnitude of several thousands of euros/g and as QC is rather unstable and needs to be prepared freshly, it was decided to buy an UV irradiation apparatus to self-synthesize QC and its derivatives. The setup is shown in Figure B2 with all main parts highlighted. Except the reaction vessel, which has been bought from proQuarz GmbH ([www.proquarz.de](http://www.proquarz.de)), all other components have been ordered from Peschl Ultraviolet GmbH ([www.peschl-ultraviolet.com](http://www.peschl-ultraviolet.com)). For power supply, a ballast unit is necessary; its technical data are listed in the following table:

Mains voltage function range	90 – 265 V
Line frequency	47 – 63 Hz
Earth leakage current 230 V, 50 – 60 Hz	< 0.7 mA
Lamp voltage range	70 – 250 V (square wave)
Lamp voltage frequency	250 Hz
Igniter voltage	4,5 kV
Open circuit voltage	250 V
Dimming range	50 -100%, dependent on lamp type
Efficiency	0.88 at 230 V / 0.85 at 115 V
Ambient temperature	max. 50 °C
Protection	Thermal cut off at 90 °C heatsink temperature Short circuit protected Open circuit protected
L / W / H	162 mm / 100 mm / 40 mm

The Hg discharge lamp needs to be cooled with water from a surrounding cooling tube. The spectral energy distribution is summarized in the following table; note that the radiation flux that hits the reaction solution depends on the transmission of the glass material (tube for lamp and cooling tube) in between:

## B Appendix

---

$\lambda$ [nm]	Radiation flux [W]
238/240	1
248	0.7
254	4
265	1.4
270	0.6
275	0.3
280	0.7
289	0.5
297	1
302	1.8
313	4.3
334	0.5
366	6.4
390	0.1
405/408	3.2
436	4.2
492	0.1
546	5.1
577/579	4.7

As neat QC has its maximum absorption band at 313 nm (without a photosensitizer) and the lamp has one of its intensity maxima also at 313 nm, the overlap is quite well.

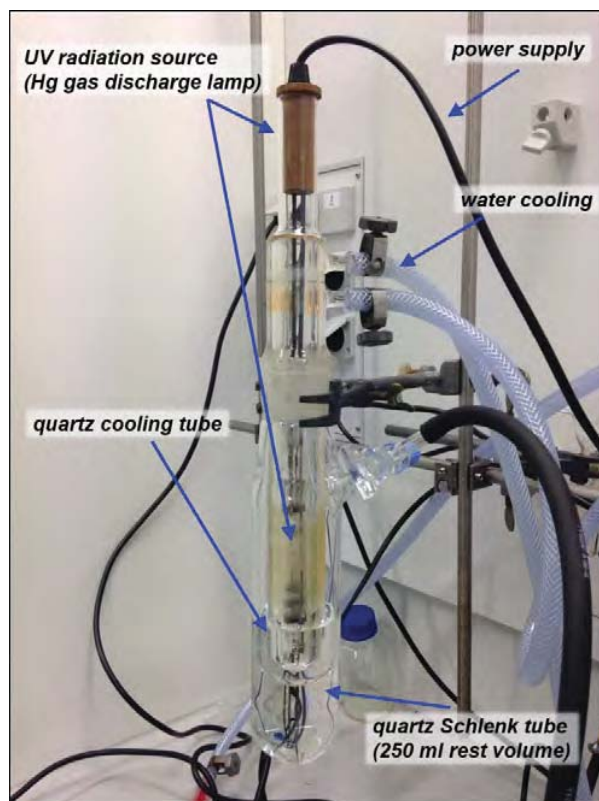


*Figure B2: Picture of the UV irradiation apparatus.*

In the following, a typical stepwise procedure for photochemical production of quadricyclanes from norbornadienes under inert conditions with the apparatus is described:

1. The quartz Schlenk tube is heated under vacuum and afterwards flushed with nitrogen. This procedure is performed twice.
2. Solvents, educts and sensitizer are added into the Schlenk tube.
3. The mixture is frozen in liquid nitrogen and vacuum is applied.
4. The mixture is slowly warmed with a water bath (50 – 60 °C) to room temperature while still kept under vacuum. During this process, dissolved gas (mostly oxygen) is bubbling out of the solution.
5. The tube is vented with a constant nitrogen stream and the solution is again frozen with liquid nitrogen.
6. When the solution is solid again, vacuum is applied and it is proceeded from step 4.

7. These freeze-pump-thaw cycles are performed until no more gas is bubbling from the solution. A complete degassing is important, as oxygen has proved to be the main initiator for multiple side reactions.
8. After degassing, the solution can be irradiated. The irradiation time depends on several parameters like solvent, the NBD compound to be converted and its concentration, photosensitizer and its concentration, and reaction volume. Typical irradiation times are in the order of several hours to several days. For irradiation, the lamp must be cooled using the attached water cooling, and all quartz tubes should be covered with aluminum foil for good reflection (shorter irradiation times), and eye protection, as the emitted radiation is very intense.
9. The reaction mixture is distilled afterwards to remove the solvent (rotary evaporator). In case of acetophenone as photosensitizer, distillation is sufficient for purification, as quantitative conversion is typically achieved under inert conditions. Other photosensitizers, e.g. Michler's ketone, possibly need further purification steps.

## Literature

1. Technical data sheet of CUN6AF4A, <https://www.neumueller.com/de/artikel/cun6af4a#> (accessed 29.06.2018).